Chemical Engineering Science 267 (2023) 118310

Contents lists available at ScienceDirect

Chemical Engineering Science

journal homepage: www.elsevier.com/locate/ces

Computational fluid dynamics simulations of phase separation in dispersed oil-water pipe flows

Jianhua Chen [a,d], Charitos Anastasiou [b], Sibo Cheng [c], Nausheen Mehboob Basha [a], Lyes Kahouadji [a], Rossella Arcucci [c,e], Panagiota Angeli [b,*], Omar K. Matar [a,*]

[a] Department of Chemical Engineering, Imperial College London, South Kensington Campus, London SW7 2AZ, United Kingdom
[b] ThAMeS Multiphase, Department of Chemical Engineering, University College London, London WC1E 7JE, United Kingdom
[c] Data Science Institute, Department of Computing, Imperial College London, London SW7 2AZ, United Kingdom
[d] State Key Laboratory of Multiphase Complex Systems, Institute of Process Engineering, Chinese Academy of Sciences, Beijing 100190, China
[e] Department of Earth Science & Engineering, Imperial College London, London SW7 2AZ, United Kingdom

HIGHLIGHTS

- Investigate separation characteristics by CFD simulations in concert with experiments.
- Find the sensitivity of the blending treatment in the solver.
- Emphasise the impact of the dense packed layer (DPL) and phase inversion on phase separation.
- Reveal the influence of the turbulent dispersion force on the flow pattern.
- Identify the feasibility of modelling the continuous phase diameter to improve the prediction.

GRAPHICAL ABSTRACT

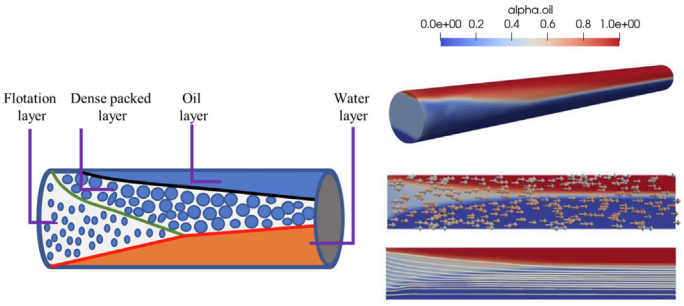

ARTICLE INFO

Article history:
Received 11 August 2022
Received in revised form 15 October 2022
Accepted 12 November 2022
Available online 28 November 2022

Keywords:
Oil-water flow
Droplet coalescence
Separation characteristics
Dense packed layer
Blending

ABSTRACT

The separation of liquid–liquid dispersions in horizontal pipes is common in many industrial sectors. It remains challenging, however, to predict the separation characteristics of the flow evolution due to the complex flow mechanisms. In this work, Computational Fluid Dynamics (CFD) simulations of the silicone oil and water two-phase flow in a horizontal pipe are performed. Several cases are explored with different mixture velocities and oil fractions (15%-60%). OpenFOAM (version 8.0) is used to perform Eulerian-Eulerian simulations coupled with population balance models. The 'blending factor' in the *multiphaseEulerFoam* solver captures the retardation of the droplet rising and coalescing due to the complex flow behaviour in the dense packed layer (DPL). The blending treatment provides a feasible compensation mechanism for the mesoscale uncertainties of droplet flow and coalescence through the DPL and its adjacent layers. In addition, the influence of the turbulent dispersion force is also investigated, which can improve the prediction of the radial distribution of concentrations but worsen the separation characteristics along the flow direction. Although the simulated concentration distribution and layer heights agree with the experiments only qualitatively, this work demonstrates how improvements in drag and coalescence modelling can be made to enhance the prediction accuracy.

* Corresponding authors.
E-mail addresses: p.angeli@ucl.ac.uk (P. Angeli), o.matar@imperial.ac.uk (O.K. Matar).

https://doi.org/10.1016/j.ces.2022.118310
0009-2509/

Nomenclature

c	coalescence rate, $m^{-3}\ s^{-1}$
C_D	drag coefficient, dimensionless
C_L	lift coefficient, dimensionless
C_{TD}	turbulent dispersion coefficient, dimensionless
C_{VM}	virtual mass coefficient, dimensionless
C_{WL}	wall lubrication coefficient, dimensionless
D	pipe diameter, m
d	droplet diameter, m
d_{320}	initial Sauter mean diameter, m
d_{32}	Sauter mean diameter, m
Eo	Eotos number, dimensionless
f	blending coefficient, dimensionless
h	layer height, m
k	turbulent kinetic energy, $m^2\ s^{-2}$
h_{C0}	layer height for the continuous water at the inlet, m
h_{O0}	layer height for the continuous oil at the inlet, m
h_{P0}	layer height for the dense packed layer at the inlet, m
$\mathbf{M}$	momentum exchange term, $N\ m^3$
p	pressure, Pa
P_b	droplet breakup probability, dimensionless

Greek letters

ϵ_{oF}	minimum volume fraction for fully continuous oil phase, dimensionless
ϵ_{oP}	minimum volume fraction for partly continuous oil phase, dimensionless
ϵ_o	oil phase volume fraction, dimensionless
ϵ_{wF}	minimum volume fraction for fully continuous water phase, dimensionless
ϵ_{wP}	minimum volume fraction for partly continuous water phase, dimensionless
ϵ_w	water phase volume fraction, dimensionless
λ	character size of eddy, m
μ	liquid dynamic viscosity, $Pa \cdot s$
ω	collision frequency, $m^{-3}\ s^{-1}$
ρ	density, $kg\ m^{-3}$
σ	surface tension, $N\ m^{-1}$
ϵ	turbulent energy dissipation rate, $m^2\ s^{-3}$
Ω_p	partial breakup rate, $m^{-3}\ s^{-1}$
Ω_t	total breakup rate, $m^{-3}\ s^{-1}$
$\boldsymbol{\tau}$	shear stress tensor, $N\ m^{-2}$

Abbreviations

CFD	Computational Fluid Dynamics
DPL	Dense Packed Layer
PBE	Population Balance Equations
PBM	Population Balance Model
TFM	Two-Fluid Model
VOF	Volume of Fluid

Subscripts

C	continuous water phase
O	continuous oil phase
P	dense packed layer
m	mixture phase
o	oil phase
w	water phase

1. Introduction

Liquid–liquid two-phase flows are widely encountered in the chemical and energy industries but it remains challenging to predict the flow patterns and separation characteristics. This is due to multiple controlling factors such as operating conditions, geometrical parameters, and physical properties such as density, viscosity, and interfacial tension (Ahmed and John, 2018; Kamp et al., 2017). Nevertheless, flow patterns in horizontal pipes have received considerable attention, and several regimes have been identified by different researchers (Trallero, 1995; Angeli, 1996; Angeli and Hewitt, 2000; Nädler and Mewes, 1997; Brauner, 2001; Xu, 2007; Ibarra et al., 2015). Although there have been slight differences in their identification nomenclatures, in general, three flow patterns might be observed: separated (or stratified) flow, fully dispersed flow (interchangeable role of the two phases), and semi-dispersed or semi-continuous flow with various sub-modes in terms of mixing layers and intermittent interfaces. In horizontal pipe separators of initially dispersed oil-in-water two-phase flows, four layers might be observed from the top of the pipe: coalesced continuous oil, dense packed layer (DPL), flotation layer, and continuous water. The rate of flotation depends on the droplet size and the holdup of the dispersed phase. If droplet flotation is faster than drop-interface coalescence, the droplets will accumulate in the dense-packed zone, in which the droplet size grows due to coalescence. The interfacial coalescence rate depends on the final droplet size and height of the DPL. In contrast, binary drop or drop-drop coalescence hardly occur in the flotation layer.

There are many experimental studies on coalescence for oil–water systems. Dong et al. (2019) studied the coalescence between a droplet and the liquid interface of its continuous homophase by using a planar laser-induced fluorescence (PLIF) technique and a fluorescent surfactant. Weheliye et al. (2017) studied the droplet coalescence with a flat interface in the presence of surfactants by using Particle Image Velocimetry (PIV). Ismail et al. (2015) summarized typical experimental systems of oil–water flows in horizontal pipes. Khatri et al. (2011) reported that surfactant can increase the emulsion stability and reduce the coalescence rate. Schumann et al. (2016) utilized a focused beam reflectance measurement probes (FBRM) to measure the droplet size distribution in water-in-oil dispersed flow in a 10 cm-ID horizontal pipe. They found that droplet size profiles in water-in-oil dispersions show a stratification over the cross-section, which is different from oil-in-water dispersions. Yu et al. (2020) developed a method of swept-frequency ultrasound attenuation to measure the oil fraction in pipes. Nguyen et al. (2017) conducted experimental and modeling studies of droplet deposition and coalescence in curved pipes, and employed an empirical correlation for droplet size distribution.

In order to describe and predict the dynamics of the layers that form when dispersed liquid–liquid flows separate, in either batch separators or continuous flow pipes, modeling work can be carried out (e.g., Hartland and Jeelani, 1988; Jeelani and Hartland, 1998; Jeelani et al., 1999; Henschke et al., 2002; Pereyra et al., 2013; Weber, 2021), and population balance equations (PBE) can be used to incorporate the effects of droplet size distribution (Cunha et al., 2008; Grimes, 2012; Grimes et al., 2012). Hu et al. (2006) developed a method to predict phase inversion in liquid–liquid flows by combining an equal surface energy criterion with PBE modelling. Weber (2021) also proposed energy consumption as a criterion for modeling liquid–liquid separation or other gravity-driven multiphase flows. Kopriwa et al. (2012) reviewed drop-population balance models for extraction columns, which can be

relevant for horizontal pipes. According to previous works, the separation is influenced by the droplet coalescence rate, especially in the DPL.

The influence of the DPL needs special consideration in the modeling work. For instance, Cunha et al. (2008) assumed the interfacial coalescence rate is proportional to the height of DPL, while Grimes (2012) calculated the interfacial coalescence time from appropriate film drainage models which would be specific to the studied systems. Lobo et al. (1993) proposed a film drainage time model which depends on the buoyancy force in the DPL with considerable thickness, and a coalescence model for small droplets (< 100 μm). The DPL behaviour has also attracted research attention in gas–liquid flow systems, such as in the metallurgical slag foaming processes (Wang et al., 2020) and in the CANMET reactors (Guitian and Joseph, 1998), where the foam layer can significantly impact the process safety and efficiency.

Computational fluid dynamics (CFD) has been used to study the flow and separation behaviour of oil–water dispersed flows (Laleh et al., 2012; Oshinowo et al., 2016), and the population balance model (PBM) has been used widely to describe the droplet size distribution (Kharoua et al., 2013; Oshinowo et al., 2016). Oshinowo and Vilagines (2020) simulated water-in-oil emulsions by using an Eulerian multiphase model, where the emulsion viscosity depends on the local droplet size distribution, which permits the prediction of the DPL thickness. Panjwani et al. (2015) investigated the water-in-oil separation process by experiments and simulations and highlighted the DPL coalescence modeling. They adopted different sub-models for the sedimentation layer, the DPL, the binary coalescence, and the interfacial coalescence. They also pointed out that droplet movement in the DPL is dominated by the momentum exchange between the two phases. Therefore, in their work, an *ad hoc* modification of the drag force based on the Hartland-type model (Jeelani and Hartland, 1985) was used, and the binary coalescence kernels were closed by models (Grimes, 2012; Grimes et al., 2012), while interfacial coalescence was modeled by a water release rate and a phase inversion criterion.

Li and Christian (2017) studied droplet breakage and coalescence of turbulent liquid–liquid flows in stirred tank reactors, and used a multi-fractal model for breakage and coalescence through a variant of the quadrature method of moments, which was coupled to the PBM within a two-fluid model (TFM). Pouraria et al. (2021) simulated dispersed water-in-oil flow in horizontal pipes by using CFD-PBM and predicted the Sauter mean diameter well. In the simulation of emulsion in a rotor–stator device, the droplet breakage rate was corrected by a mesoscale model to improve the prediction of droplet size distribution (Chen et al., 2019). Eulerian simulations of liquid–liquid dispersions in pump facilities have also been reported (Valdés et al., 2021; Zhou et al., 2021), in which the PBM kernels were deliberately selected based on the specific platforms. In certain studies, coalescence is neglected in the CFD-PBM simulation of dilute or high-turbulence dispersions (Eskin and Vikhansky, 2019; Maluta et al., 2021). In addition, Shi et al. (2021) conducted a Volume-of-Fluid multiphase simulation of high viscosity ratio oil–water flows, which predicted the flow patterns well.

From the above literature review, it is clear that predicting the separation characteristics of oil–water dispersed flow, either in batch separators or in pipelines, remains a challenge. Batch mode mechanistic models usually require an input of key parameters that are specific to given systems. On the other hand, the CFD-PBM simulation provides a versatile framework, because of the layer-specific behaviour, e.g., mesoscale structures of packing droplets and draining films; the PBM kernels would also require parameter fittings for specific multiphase flow systems. In the present work, we carry out a study that employs OpenFOAM CFD simulations coupled to PBM. We demonstrate the use of the so-called 'blending factor' in *multiphaseEulerFoam* in modelling the retardation of drop rise and coalescence within the DPL and in capturing the separation characteristics of oil-in-water dispersed flows in horizontal pipes.

The rest of this paper is organised as follows. Section 2 presents the physical setup and the numerical method in detail. The results and discussion are presented in Section 3 focusing on the concentration profiles and layer heights of the separating flow, as well as the influence of the blending treatment and the turbulent dispersion force in the simulation. Finally, Section 4 gives concluding remarks of the present work.

2. Problem formulation and simulation methods

In this section, we provide details of the numerical methodology used to model the two-phase flow dynamics that accompany the separation of oil-and-water dispersed flows in horizontal pipelines. We begin by providing a concise description of the physical setup which is modelled in the present work; this setup is also used to generate the data utilised to inform and validate the numerical predictions.

2.1. Physical setup

The experiments were conducted with the flow rig developed by Voulgaropoulos (2018). The flow rig consisted of two horizontal 7 m long and 37 mm diameter (±0.3 mm) acrylic pipes which are connected by a U-bend. The oil phase was introduced to the pipe through a multi-nozzle inlet in order to create an oil-in-water dispersion. Conductivity measurements with dual-conductance probes were implemented at axial measuring locations (20D, 65D, 80D, 135D and 150D, where D is the pipe diameter) in the front pipe of the flow rig, to study the droplet size and layer evolution. Measurements were taken for every $\Delta y = 0.054D$ in the vertical direction of the pipe cross-sectional, and the vertical time-averaged oil fraction profiles obtained from the conductance probes for $\Delta t = 10$ s were used in this work.

Several cases were explored with different mixture velocities (0.52 and 1.04 m/s) and input oil concentration (15%, 30%, 45% and 60%), and the experimental results of the oil concentration profiles and evolving layer heights were collected to validate the simulations; the parameters can be found in Tables 1 and 2. In Table 2, h_{C0}, h_{O0} and h_{P0} are the layer heights at the inlet for the continuous water, the continuous oil and the dense packed layer respectively. The last three columns of Table 2 show the measured Sauter mean diameter of the oil droplets at the inlet ($x = 0$), $x = 65D$, and $x = 135D$ respectively. Layer boundaries were defined through the oil concentration profiles; following Voulgaropoulos (2018) the boundary for the DPL is set at 0.90 oil fraction.

2.2. Governing equations of the Eulerian framework

The oil and water phases are taken to be incompressible, Newtonian, and immiscible, of constant density and viscosity, and a well-defined interfacial tension. The equations of mass and momentum conservation are respectively expressed by

$$\frac{\partial}{\partial t}\left(\epsilon_k\ \rho_k\right) + \nabla\cdot\left(\epsilon_k\ \rho_k\ \mathbf{U}_k\right) = 0, \tag{1}$$

$$\frac{\partial}{\partial t}(\epsilon_k\rho_k\mathbf{U}_k) + \nabla\cdot(\epsilon_k\rho_k\mathbf{U}_k\mathbf{U}_k) = -\epsilon_k\nabla p + \nabla\cdot(\epsilon_k\boldsymbol{\tau}_k) + \epsilon_k\rho_k\mathbf{g} + \mathbf{M}_k, \tag{2}$$

Table 1
Physical properties of the experimental system.

Liquid	Phase	ρ(kg m^{-3})	μ(Pa · s)	σ(N m^{-1})
Water	Aqueous	998	0.9×10^{-3}	~ 0.0329
Exxsol D140	Organic	828	5.5×10^{-3}	

Table 2
Operating parameters of the experiments.

U_m (ms^{-1})	ϵ_o	$h^+_{C0} = h_{C0}/D$	$h^+_{O0} = h_{O0}/D$	$h^+_{P0} = h_{P0}/D$	d_{320} (mm)	$d_{32}\|_{65D}$ (mm)	$d_{32}\|_{135D}$ (mm)
0.52	0.30	0.405	1.0	0.76	3.41	3.50	3.90
0.52	0.45	0.365	0.811	0.65	4.03	4.27	4.33
0.52	0.60	0.27	0.703	0.59	4.25	4.35	4.56
1.04	0.15	0.405	1.0	0.92	1.14	1.31	1.42
1.04	0.30	0.189	1.0	0.92	1.27	1.45	1.65
1.04	0.60	0.122	1.0	0.81	2.43	2.56	2.74

where the subscript of k = o, w represents the water and oil phases, respectively, and $\boldsymbol{\tau}$ is the stress tensor:

$$\boldsymbol{\tau}_k = \mu_{eff}\left[\nabla \mathbf{U}_k + (\nabla \mathbf{U}_k)^T - \frac{2}{3}(\nabla \cdot \mathbf{U}_k)\mathbf{I}\right]. \tag{3}$$

The rate of momentum transfer per unit volume between the phases, $\mathbf{M}_k$, consists of several terms that would be caused by drag, lift, virtual mass, turbulent dispersion, and wall lubrication forces:

$$\mathbf{M}_o = -\mathbf{M}_w = \mathbf{M}_o^D + \mathbf{M}_o^L + \mathbf{M}_o^{VM} + \mathbf{M}_o^{TD} + \mathbf{M}_o^{WL}. \tag{4}$$

The individual terms can be expressed as below, and more details can be found from references (Deen et al., 2001; Lopez de Bertodano, 1992; Cheng et al., 2018):

$$\mathbf{M}_o^D = \frac{3}{4}\epsilon_o \rho_w \frac{C_D}{d_o}|\mathbf{U}_w - \mathbf{U}_o|(\mathbf{U}_w - \mathbf{U}_o), \tag{5}$$

$$\mathbf{M}_o^L = -\epsilon_o \rho_w C_L(\mathbf{U}_w - \mathbf{U}_o) \times (\nabla \times \mathbf{U}_w), \tag{6}$$

$$\mathbf{M}_o^{VM} = \epsilon_o \rho_w C_{VM}\left(\frac{D\mathbf{U}_w}{Dt} - \frac{D\mathbf{U}_o}{Dt}\right), \tag{7}$$

$$\mathbf{M}_o^{TD} = -\rho_w k_w C_{TD} \nabla \epsilon_o, \tag{8}$$

$$\mathbf{M}_o^{WL} = -\epsilon_o \rho_w \max\left(C_{w1} + C_{w2}\frac{R_o}{y}, 0\right)\frac{|\mathbf{U}_r - (\mathbf{U}_r \cdot \mathbf{n}_w)\mathbf{n}_w|^2}{R_o}\mathbf{n}_w, \tag{9}$$

where d_o and R_o are the oil droplet diameter and radius, respectively, $\mathbf{n}_w$ is the outward facing unit vector on the wall, and y is the distance from the wall. The drag coefficient C_D is calculated by the distorted droplet drag model from (Ishii and Zuber, 1979):

$$C_D = \frac{2}{3}\sqrt{\frac{g(\rho_w - \rho_o)d_o^2}{\sigma}}\left\{\frac{1 + 17.67[f(\epsilon_o)]^{6/7}}{18.67 f(\epsilon_o)}\right\}^2, \tag{10}$$

$$f(\epsilon_o) = \sqrt{1 - \epsilon_o}\left(\frac{\mu_w}{\mu_m}\right), \tag{11}$$

$$\frac{\mu_m}{\mu_w} = (1 - \epsilon_o)^{-2.5(\mu_o + 0.4\mu_w)/(\mu_o + \mu_w)}. \tag{12}$$

As discussed in Rusche (2003), the above equations for calculating the momentum exchange are not valid to model phase inversion and separating flows, such as the gas–liquid flow in bubble columns. In those flows, the originally dispersed phase can shift to continuous phase and vice versa, then the flow parameters will swap their roles in the equations, and a diameter must be specified for the original continuous phase. To this end, OpenFOAM provides an optional blending treatment for all the interfacial forces, which enables determining the dispersed and continuous phase locally for each cell. Obviously, this work needs to include the blending treatment in order to simulate the phase separating process. The influence of blending will be discussed in Section 3.1.

The blending treatment was exerted on all the interfacial forces. For simplicity, the treatment is illustrated here by only taking the drag force as an example, and more details can be found in literature (Rusche, 2003; Li and Christian, 2017).

$$\begin{aligned}\mathbf{M}_o^D &= f_o \mathbf{M}_o^D + f_w \mathbf{M}_w^D \\ &= \frac{3}{4}\epsilon_o \epsilon_w \left(f_o \rho_w \frac{C_{Do}}{d_o} + f_w \rho_o \frac{C_{Dw}}{d_w}\right)|\mathbf{U}_w - \mathbf{U}_o|(\mathbf{U}_w - \mathbf{U}_o),\end{aligned} \tag{13}$$

where f_o and f_w are the blending coefficients for the two phases, d_o is the oil droplet diameter and d_w is the diameter of the original continuous phase which will be automatically invoked by the blending treatment. In the present work, only the oil droplet size d_o was calculated by the PBM method, and when oil is the continuous phase, a constant d_w was used as the dispersed phase diameter in the momentum exchange. It should be noted that the blending treatment considers three possible regimes of oil-in-water, water-in-oil, and water-and-oil. It works through calculated blending coefficients in the first two regimes featuring dispersed flows. While for the third regime (i.e. fully separated flow), a default segregated model (Marschall, 2011) was adopted for the drag, that is,

$$\mathbf{M}_{Segregated} = \lambda(Re_I, \pi_\mu)\frac{|\nabla \epsilon_o|}{\delta}\frac{\mu_o \mu_w}{\mu_o + \mu_w}(\mathbf{U}_o - \mathbf{U}_w), \tag{14}$$

where

$$\lambda(Re_I, \pi_\mu) = mRe_I + n\pi_\mu, \tag{15}$$

$$Re_I = \frac{\rho_w \delta |\mathbf{U}_o - \mathbf{U}_w|}{\epsilon_o \epsilon_w \mu_o \mu_w/(\mu_o + \mu_w)}, \tag{16}$$

$$\pi_\mu = \frac{\epsilon_o \epsilon_w \mu_o \mu_w/(\epsilon_o \mu_o + \epsilon_w \mu_w)}{\mu_o \mu_w/(\mu_o + \mu_w)}, \tag{17}$$

$$\delta = \frac{1}{|\nabla \epsilon_o|}. \tag{18}$$

Although the blending source code has considered three terms for the momentum exchange, denoted by

$$\mathbf{M} = f_1 \mathbf{M}_{model1In2} + f_2 \mathbf{M}_{model2In1} + (1 - f_1 - f_2)\mathbf{M}_{model}, \tag{19}$$

the third term lacks available models for most interfacial forces except the drag force, and if the condition of $f_1 + f_2 = 1$ is satisfied

(should be recommended for two-phase flows requiring the blending treatment), this term will be zero and hence can be omitted.

There are two methods for calculating the blending coefficients, i.e. linear and hyperbolic in the current solver. In the linear method, four volume fraction parameters of $\epsilon_{o,F}$, $\epsilon_{o,P}$, $\epsilon_{w,F}$, and $\epsilon_{w,P}$ need to be defined to determine the local role of each phase, thereby f_o and f_w are calculated as follows:

$$f_o = \min\left(\max\left(\frac{\epsilon_w - \epsilon_{w,P}}{\epsilon_{w,F} - \epsilon_{w,P}}, 0\right), 1\right), \tag{20}$$

$$f_w = \min\left(\max\left(\frac{\epsilon_o - \epsilon_{o,P}}{\epsilon_{o,F} - \epsilon_{o,P}}, 0\right), 1\right). \tag{21}$$

For $\epsilon_o \to 1$, water is the dispersed phase in oil, and d_w is used for calculating the drag force. Similarly, using a tanh to smooth the blending function for f_o and f_w one can write:

$$f_o = \frac{1 + \tanh\left(4/B_w(\epsilon_w - \epsilon_{w,F})\right)}{2}, \tag{22}$$

$$f_w = \frac{1 + \tanh\left(4/B_o(\epsilon_o - \epsilon_{o,F})\right)}{2}, \tag{23}$$

where B_o and B_w represent the phase transition parameters, and $\epsilon_{o,F}$ and $\epsilon_{w,F}$ are volume fraction parameters.

The lift coefficient can be modeled by Tomiyama et al. (2002):

$$C_L = \begin{cases} \min\left(0.288\tanh\left(0.121Re_b\right), f(Eo)\right) & \text{if } Eo < 4 \\ f(Eo) & \text{if } 4 \leqslant Eo \leq 10.7 \end{cases} \tag{24}$$

$$f(Eo) = 0.00105Eo^3 - 0.0159Eo^2 - 0.0204Eo + 0.47. \tag{25}$$

The virtual mass force is neglected in the present work, considering that the density difference between oil and water is much smaller compared to gas–liquid flows.

There are several models for the turbulent dispersion force, and more details can be found in the literature (Wang and Yao, 2016; Pouraria et al., 2021). At first, the turbulent dispersion force is not included to simplify the exploration of the blending effects, then its effect is studied in Section 3.2. The wall lubrication force is modeled by Antal et al. (1991) with typical coefficient values of $C_{w1} = -0.01$ and $C_{w2} = 0.05$. The mixture $k-\epsilon$ model is used to calculate the turbulent viscosity, and more details can be found in the reference (Behzadi et al., 2004; Bhusare et al., 2017; Cheng et al., 2018):

$$\frac{\partial}{\partial t}(\rho_m k_m) + \nabla\cdot(\rho_m \mathbf{U}_m k_m) = \nabla\cdot\left(\frac{\mu_m^t}{\sigma_k}\nabla k_m\right) + G_k^m - \rho_m\epsilon_m + S_k^m, \tag{26}$$

$$\begin{aligned}\frac{\partial}{\partial t}(\rho_m \epsilon_m) + \nabla\cdot(\rho_m \mathbf{U}_m \epsilon_m) = {} & \nabla\cdot\left(\frac{\mu_m^t}{\sigma_\varepsilon}\nabla\epsilon_m\right) \\ & + \frac{\epsilon_m}{k_m}\left(C_{\varepsilon1}G_k^m - C_{\varepsilon2}\rho_m\epsilon_m\right) \\ & + C_{\varepsilon3}\frac{\epsilon_m}{k_m}S_k^m,\end{aligned} \tag{27}$$

where the source term S_k^m was calculated by the model proposed in Lahey (2005), that is,

$$S_k^m = C_p\left(1 + C_D^{4/3}\right)\epsilon_o\frac{|\mathbf{U}_w - \mathbf{U}_o|^3}{d_o}, \tag{28}$$

with $C_p = 0.25$. The mixture variables were calculated based on the volume-averaged method for each phase (Cheng et al., 2018). This model was recommended by Behzadi et al. (2004) for modelling dispersed bubble and droplet flows at high phase factions. The model can be applied to all phase fraction values and it can also reduce to the single phase model. When the phase fraction is higher than the limit value (e.g., $\geqslant 6\%$), the response function, which means the ratio of velocity fluctuations between the dispersed and continuous phase, approaches a constant value, indicating that both phases fluctuate as one entity and hence the mixture assumption becomes reasonable. Since the studied flow system undergoes phase inversion with high concentration ($\geqslant 15\%$), it should be suitable to use the mixture $k-\epsilon$ turbulence model in this work.

2.3. Population balance model

The class method developed by Kumar and Ramkrishna (1996) is used to solve the population balance model of the droplet. A series of droplet classes are specified and the population balance equations are expressed as below. The so-called binaryBreakupModels algorithm developed by Liao et al. (2018) is used for calculating the breakup.

$$\frac{\partial(\epsilon_o f_i)}{\partial t} + \nabla\cdot(\epsilon_o \mathbf{U}_o f_i) = S_i, \tag{29}$$

where S_i is the source term for droplet coalescence and breakup,

$$\begin{aligned} S_i = & \sum_{j,k}^{j\geqslant k}(1-\tfrac{1}{2}\delta_{jk})\eta c(x_j,x_k)\tfrac{\epsilon_o f_j}{x_j}\tfrac{\epsilon_o f_k}{x_k}x_i - \epsilon_o f_i\sum_{k=1}^{M}c(x_j,x_k)\tfrac{\epsilon_o f_k}{x_k} \\ & x_{i-1} \leqslant (x_j + x_k) \leqslant (x_{i+1}) \\ & + \sum_{j=i}^{M}\epsilon_o f_j\left[\Omega_p(x_i,x_j)\Delta v_i(j) + \sum_{k=1}^{M}\Omega_p(x_k,x_j)Y_{ijk}\Delta v_k(j)\right] - \epsilon_o f_i\sum_{j=1}^{i}\Omega_p(x_j,x_i)\Delta v_j(i), \end{aligned} \tag{30}$$

$$\eta = \begin{cases} \frac{x_{i+1}-v}{x_{i+1}-x_i} & x_i \leqslant v \leqslant x_{i+1} \\ \frac{v-x_{i-1}}{x_i-x_{i-1}} & x_{i-1} \leqslant v \leqslant x_i \end{cases}, \tag{31}$$

$$Y_{ijk} = \begin{cases} \frac{(x_j-x_k)-x_{i-1}}{x_i-x_{i-1}}, & \text{if } x_{i-1} \leqslant x_j - x_k < x_i \\ \frac{x_{i+1}-(x_j-x_k)}{x_{i+1}-x_i}, & \text{if } x_i \leqslant x_j - x_k < x_{i+1} \\ 0, & \text{else} \end{cases}, \tag{32}$$

$$\Delta v_i(j) = \begin{cases} v_{i+1} - v_i, & \text{if } v_{i+1} \leqslant x_j/2 \\ x_j/2 - v_i, & \text{if } v_i < x_j/2 < v_{i+1} \\ 0, & \text{if } v_i \geqslant x_j/2 \end{cases}, \tag{33}$$

where $c(x_j,x_k)$ is the coalescence rate, and $\Omega_p(x_j,x_i)$ is the partial breakup rate. In the present work, the Prince and Blanch (1990) model is used as the coalescence kernel and the Luo and Svendsen (1996) as the breakup kernel. A concise description of the model equations is given hereafter and more details can be found in the reference (Liao and Lucas, 2010; Liao et al., 2018) and "C++ Source Code Guide" of OpenFOAM (version 8).

The partial breakup rate is calculated by the following expression

$$\begin{aligned}\Omega_p(x_j,x_i) = {} & 0.923(1-\epsilon_o)\left(\frac{\epsilon}{d_i^2}\right)^{1/3}\times\int_{\xi_{min}}^{1}\frac{(1+\xi)^2}{\xi^{11/3}} \\ & \times\exp\left(-\frac{12c_f\sigma}{2\rho_w\epsilon^{2/3}d_i^{5/3}\xi^{11/3}}\right)d\xi,\end{aligned} \tag{34}$$

and the total breakup rate of droplet class i can be obtained by

$$\Omega_t(x_i) = \sum_{j=1}^{i}\Omega_p(x_j,x_i)\Delta v_i(j), \tag{35}$$

and ξ_{min} and c_f are respectively expressed by

$$\xi_{\min} = \frac{11.4}{d_i}\left[\frac{(\mu_w/\rho_w)^3}{\epsilon}\right]^{0.25}, \tag{36}$$

$$c_f = \left(\frac{v_j}{v_i}\right)^{2/3} + \left(1 - \frac{v_j}{v_i}\right)^{2/3} - 1. \tag{37}$$

The coalescence rate is calculated by multiplying with the collision frequency $\omega(d_i, d_j)$ and coalescence efficiency $P(d_i, d_j)$, and the former accounts for turbulence, buoyancy, and laminar shear, denoted by ω^T, ω^B, and ω^{LS}, respectively:

$$c(d_i, d_j) = \omega(d_i, d_j)P(d_i, d_j), \tag{38}$$

$$\omega(d_i, d_j) = \omega^T(d_i, d_j) + \omega^B(d_i, d_j) + \omega^{LS}(d_i, d_j), \tag{39}$$

$$\omega^T(d_i, d_j) = \frac{\pi}{4}\sqrt{2}\epsilon_w^{1/3}(d_i + d_j)^2\left(d_i^{2/3} + d_j^{2/3}\right)^{1/2}, \tag{40}$$

$$\omega^B(d_i, d_j) = \frac{\pi}{4}(d_i + d_j)^2\left|u_i^r - u_j^r\right|, \tag{41}$$

$$\omega^{LS}(d_i, d_j) = \frac{1}{6}(d_i + d_j)^3\dot{\gamma}_w, \tag{42}$$

where ϵ_w is the turbulent energy dissipation rate, $\dot{\gamma}_w$ is the shear strain rate of the continuous phase, and u_i^r is the rise velocity of bubble i:

$$u_i^r = \sqrt{\frac{2.14\sigma}{\rho_w d_i} + 0.505 g d_i}. \tag{43}$$

The coalescence efficiency is expressed as

$$P(d_i, d_j) = \exp\left\{-\sqrt{\frac{r_{ij}^3\rho_w}{16\sigma}}\ln\left(\frac{h_0}{h_f}\right)\epsilon_w^{1/3}r_{ij}^{-2/3}\right\}, \tag{44}$$

in which r_{ij} is given by

$$r_{ij} = \left(\frac{1}{d_i} + \frac{1}{d_j}\right)^{-1}, \tag{45}$$

with the coefficients of $h_0 = 10^{-4}$ and $h_f = 10^{-8}$.

2.4. Simulation implementation

The multiphaseEulerFoam solver in OpenFOAM (version 8.0) was used for the coupled Eulerian-Eulerian simulations and the PBM equations. Physical properties can be found in Table 1. Structured meshes were generated by the utility of *blockMesh*. Since the experimental measurements were performed on the first 7 m length pipe, only this part was selected as the simulations domain. According to Table 2, the flow parameters at the inlet for the simulation can be defined. That is, the inlet was split into three patches corresponding to the values of h_{C0}, h_{O0} and h_{P0}, in which the mixture velocity U_m was set for both phases, and the volume fractions of ϵ_o and ϵ_w for each patch were calculated based on the average oil concentration and the area ratios. By this way, the flow parameters in simulations approximate the experimental setup well. At the inlet, the *fixedFluxPressure* condition was adopted for pressure, which set the pressure gradient such that the flux was consistent with the velocity boundary condition. In all cases, the mixture $k-\epsilon$ model was used for the turbulent equations. The turbulent intensity was estimated by an empirical correlation (Pouraria et al., 2021),

$$I = 0.16Re^{(-1/8)}. \tag{46}$$

As to the size distribution in PBM, it consisted of 22 size bins ranged in 1–5 mm. Two kinds of setup were tested for the initial size fractions: one is a uniform size class fraction of 0.05 for all the 20 classes except the two endpoints; the other is a dominating fraction of 0.9 for the size class most close to the initial diameter d_{320}, along with smaller fractions of 0.05 for the two adjacent sizes. Preliminary simulations demonstrated that the results were insensitive to the initial distribution, so the non-uniform distribution was used for all cases. The transient PIMPLE algorithm was used to solve pressure–velocity coupling. The generalised geometric-algebraic multi-grid (*GAMG*) solver along with the *DIC* smoother was used to solve the pressure equation, while the *smoothSolver* combined with *symGaussSeidel* smoother were used for solving the other equations. More details about the boundary conditions and discretization schemes can be found in Tables 3,4.

The blending parameters adopted the default values $\epsilon_{o,F} = \epsilon_{w,F} = 0.7$ and $\epsilon_{o,P} = \epsilon_{w,P} = 0.3$; the effect of the blending function on the results will also be discussed. The droplet diameter of the continuous phase was first set arbitrarily as d_w = 0.5 mm; its effect will also be discussed in the following sections since it has a significant impact on the simulation results. In order to obtain a steady flow pattern, the flow time is set as 16 s for U_m = 0.52 m/s and 10 s for U_m = 1.04 m/s. Adaptive time steps were used in order to ensure the convergence, and a time step of 0.0025 s worked well for cases with medium grid resolution. The running time was 80–100 h for each case on a four-nodes parallel computing mode. All simulations were performed on the high-performance computing system (Intel® Xeon(R) CPU E5-2620, 2.00 GHz, RAM 64 GB). Regarding the influence of the grid resolution, three meshes with 180000, 345600, and 720000 cells were compared for the case of U_m = 1.04 m/s and ϵ_o = 0.3.

Fig. 1 shows the flow rig reported in Voulgaropoulos (2018) and a snapshot of a typical flow development along the pipe for the case of U_m = 1.04 m/s and ϵ_o = 0.3. The separation behaviour in the flow pipe can be observed through the oil concentration, where red colour indicates oil and blue indicates water. The flow velocity vectors and streamlines provide insight into the structure of the velocity field. Fig. 2 depicts the variation of the oil volume fraction with the normalised vertical direction for three axial stations along the pipe, $x/D = 20, 80, 150$, for the same parameters as in Fig. 1.

Table 4
The discretization schemes.

Modeling terms	Keywords of Schemes	Schemes
Convection terms	divSchemes	Gauss vanLeer
Gradient terms	gradSchemes	Gauss linear
Diffusive terms	laplacianSchemes	Gauss linear uncorrected
Time derivative	ddtSchemes	Euler
Others	interpolationSchemes	linear
	snGradSchemes	uncorrected

Table 3
Boundary conditions.

Boundary fields	Inlet	Outlet	Walls
Phase fraction	fixedValue	inletOutlet	zeroGradient
Velocities	fixedValue	pressureInletOutletVelocity	fixedValue
Pressure	fixedFluxPressure	prghPressure	fixedFluxPressure

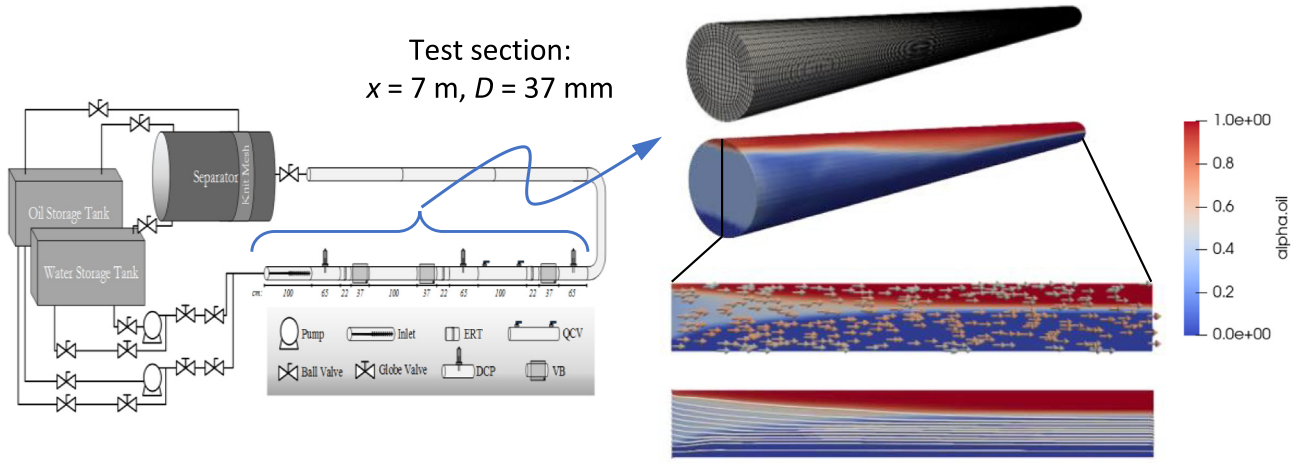

Fig. 1. The flow rig and simulation of the oil–water flow in a horizontal pipe separator for the case of U_m = 1.04 m/s and ϵ_o = 0.3, d_w = 0.5 mm. The physical and operating parameters are in Tables 1,2, and the numerical setups are listed in Tables 3,4.

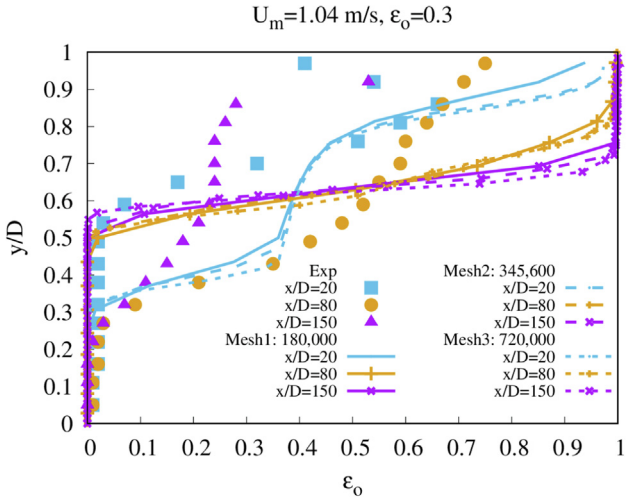

Fig. 2. The influence of the grid resolution through the concentration profiles, d_w = 0.5 mm.

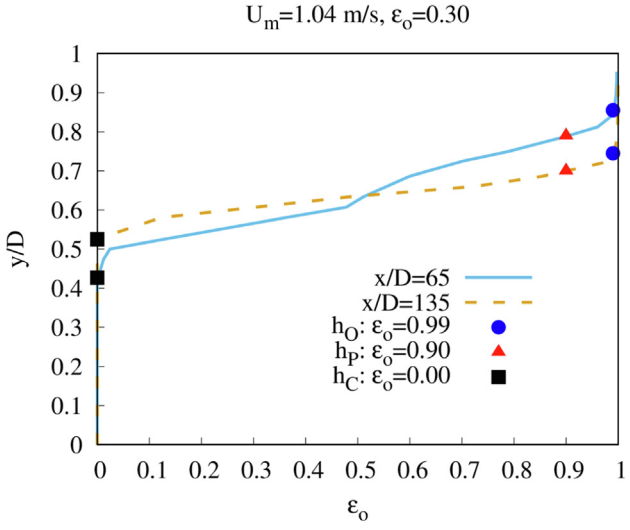

Fig. 3. The method to determine layer heights from the simulation results, d_w = 0.5 mm. h_C, h_P and h_O are layer heights of the continuous water, dense packed layer and coalesced oil, respectively.

Here, it is seen clearly that convergence of the numerical results has been achieved upon mesh refinement, and the mesh corresponding to 345,600 points ('Mesh2') is adopted for the remaining computations discussed in the present work. The deviation between the simulation results and the experimental data will be discussed in the next section.

For the simulated results, the layer heights are read from the concentration profiles at x/D = 65 and x/D =135, while three other concentration profiles are read at x/D = 20, 80 and 150, respectively. Fig. 3 shows an example for determining the layer height, where h_C, h_P and h_O are layer heights of the continuous water, dense packed layer and coalesced oil, respectively. From the perspective of layer thickness, the continuous oil layer is assumed for $\epsilon_o \geqslant 0.99$, the packed layer for $0.90 < \epsilon_o < 0.99$, and the continuous water layer as $\epsilon_o \leqslant 0$.

3. Results and discussion

3.1. Influence of blending treatment and $\mathbf{d}_w$

We begin the discussion of our results by assessing their sensitivity to the choice of d_w. When blending is invoked, the solver switches the dispersed phase diameter between d_o and d_w for calculating momentum exchange. Fig. 4 demonstrates the influence of different d_w values on the simulated oil concentration profiles in the normalised vertical direction, y/D, presented in the pipe midplane. Smaller d_w values lead to a marked difference in the ϵ_o distribution across the pipe particularly for locations downstream from the inlet. As shown in Fig. 4, the transition from the water layer to finite oil fractions occurs at lower elevations than for larger d_w values; in contrast, the transitions to the dense packed and continuous oil layers occur at higher elevations indicating retarded droplet rising in the upper region of the pipe. The sensitivity on blending is also shown in Fig. 5 for U_m = 0.52 m/s and ϵ_o = 0.3. Comparison of Figs. 5a and 5b demonstrates that the oil–water-separation takes place further upstream than the case in which blending is employed. This may be attributed to the difference of the continuous phase viscosity, recalling the phase inversion in the blending treatment. When a larger constant d_o value of 3.41 mm (i.e., in accordance with the experimental measurement) is used in the no-blending case, the separation is completed significantly closer to the inlet (see Fig. 5c) than the cases depicted in Figs. 5a and 5b. Based on these results, it is proposed that the blending treatment may compensate for the overestimated rise

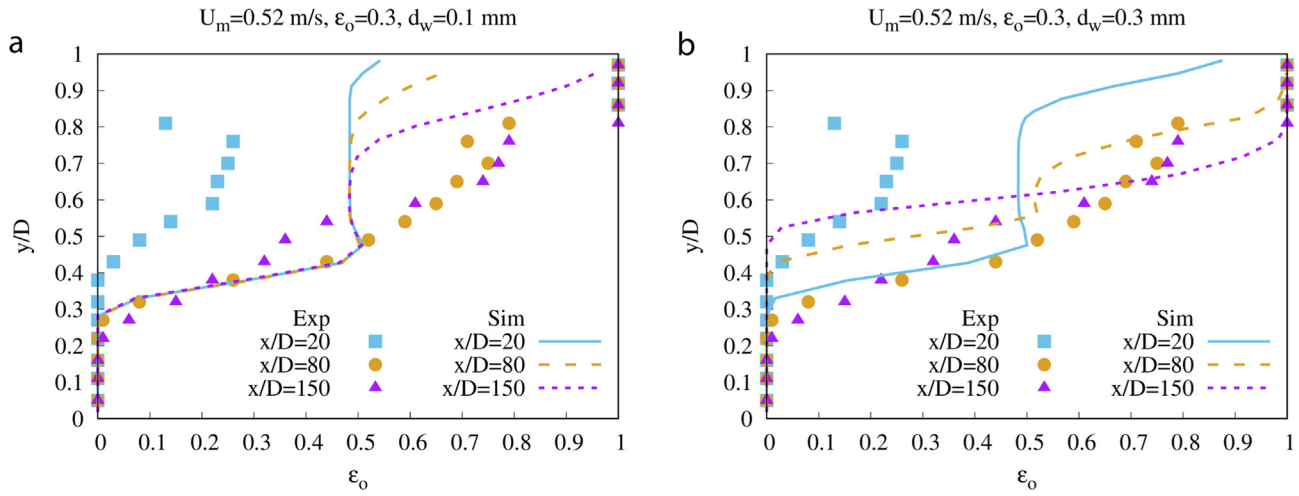

Fig. 4. Impact of the parameter of d_w on the concentration profiles.

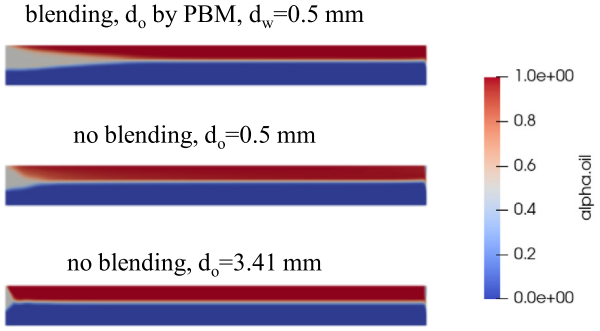

Fig. 5. Influence of the droplet diameters of d_w and d_o for the case of U_m = 0.52 m/s, ϵ_o = 0.3.

velocity and coalescence rate of the oil droplets, and will help to reduce the rate of separation.

The mechanistic model proposed by Pereyra et al. (2013) (see appendix for details) was further used for this flow system to compare with the simulations to gain insight into the factors that affect the separation, such as the order of magnitude of the coalescence time and the separation length. Fig. 6 illustrates the layer height comparison between the model calculations and the experimental results for the case of U_m = 0.52 m/s and ϵ_o = 0.45. With deceasing initial droplet diameter of d_{320}, the cross point between h_P and h_C moves towards the outlet, indicating a decreasing separation rate. When using d_{320} = 0.2 mm, the dense packed layer height of h_P are well captured by the model calculation, which verifies the feasibility of adopting a much smaller diameter than the measurement to calculate the drag force. However, the calculated h_O is not sensitive to d_{320} even though its slope changes slightly.

The results presented thus far reveal that the blending treatment can be used to improve the CFD simulation of separation characteristics. The logic of the blending treatment is consistent with the correction of emulsion viscosity (Oshinowo and Vilagines, 2020). That is, the conventional drag force should be enhanced by modifying either the viscosity of the surrounding phase or the droplet diameter, noticing that the drag is proportional to C_D/d_o. Drag can be corrected by either decreasing droplet diameter or increasing the viscosity.

A comparison between the linear and hyperbolic blending functions was also carried out. The variation of the blending coefficients is shown in Fig. 7. For the hyperbolic blending, all model

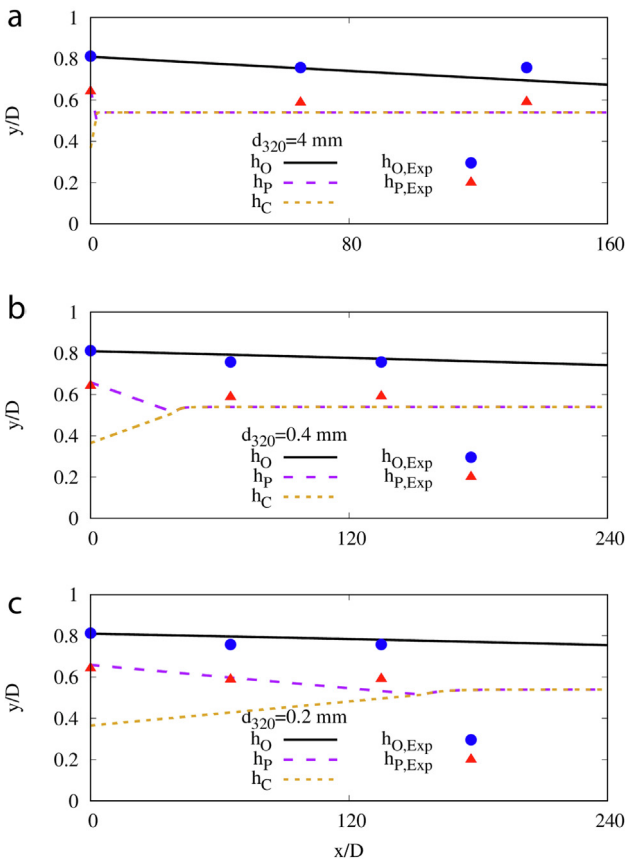

Fig. 6. Influence of the initial droplet diameter in the mechanistic model, U_m = 0.52 m/s, ϵ_o = 0.45.

parameters were set at a constant value of 0.5, while for linear blending, when one phase reached a volume fraction of 0.7, it was considered continuous. This shifting is consistent with that of the phase inversion reported in (Hu et al., 2006). Fig. 7a shows the concentration profiles along the pipe, where only marginal changes are observed for different cases between the two blending methods. This is not surprising since the blending coefficients display small differences as shown in Fig. 7(b,c). Therefore, the linear blending will be used. This section will discuss the simulation

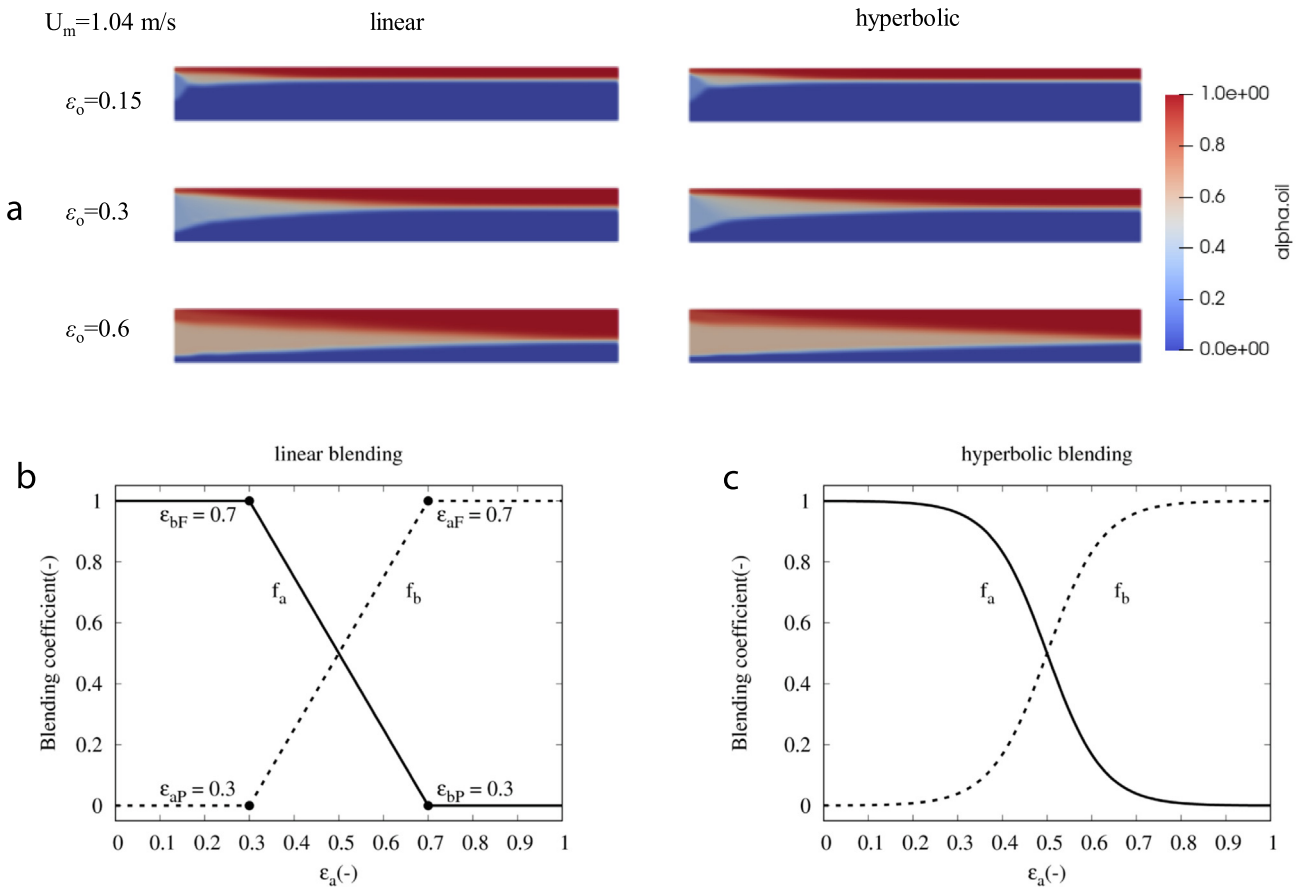

Fig. 7. The effect of the blending function employed in the present work on the concentration profiles for $\epsilon = 0.15$, 0.3, and 0.6, and with U_m = 1.04 m/s and d_w = 0.5 mm, (a); the linear and hyperbolic blending functions are shown in (b) and (c), respectively.

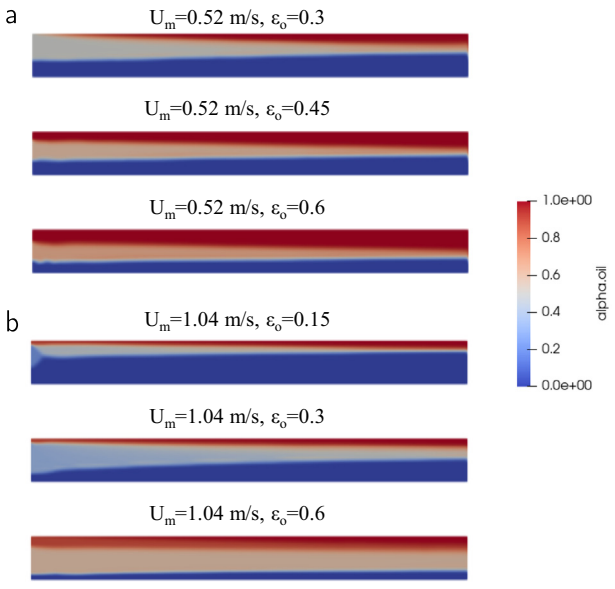

Fig. 8. Parametric dependence of the oil concentration profiles in the pipe on ϵ_o with U = 0.52 m/s, (a), and 1.04 m/s, (b), d_w = 0.25 mm.

results using linear blending with d_w = 0.25 mm. Fig. 8 shows the contour plots of the oil concentration. The dispersed regions in Fig. 8(b) take up larger proportion of the whole pipe compared to Fig. 7(a), indicating that the separation has slowed down. This result agrees with the fact that decreasing d_w augments the drag force between the two phases.

For the cases of U_m = 0.52 m/s shown in Fig. 9, the concentration profiles show better agreement between the experimental data and the numerical predictions than those of d_w = 0.5 mm. In Fig. 9(a,c,e), all the simulated curves are within the range of the measurements except for the position of x/D=20, ϵ_o = 0.3. In Fig. 9(b,d,f), three height values of the coalesced oil layer h_O, the dense packed layer h_P, and the flotation layer h_C are shown against the mechanistic model, while only the first two heights are available from the experiments. Although the simulations overestimate slightly the h_O values, they show good agreement with the mechanistic model calculations with the model lines located between the experiments and the simulations in each case. For the h_P values, the simulations are higher than the experiments, but the differences decrease with increasing oil concentration. Interestingly, the model lines agree well with the experimental h_P results at a given d_{320}. Coincidentally, the range of 0.1 ~ 0.2 mm for d_{320} is also one order of magnitude smaller than the measured droplet diameter, which corroborates the use of the modified d_w. For the h_C values, the simulated results under-predict the model lines. Since the droplets move with mild interactions in the flotation layer, the present blending treatment might lead to enlarged hindering in this region, and affect the rate of h_C increase.

For the cases of U_m = 1.04 m/s shown in Fig. 10, the predicted concentration profiles are improved in comparison to the cases using d_w = 0.5 mm (e.g., as seen in Fig. 2 for ϵ_o = 0.3), especially in the top region of the pipe. Meanwhile, the prediction of layer heights has significantly improved, though the concentration profiles are not satisfactory. h_O and h_P values show good agreement

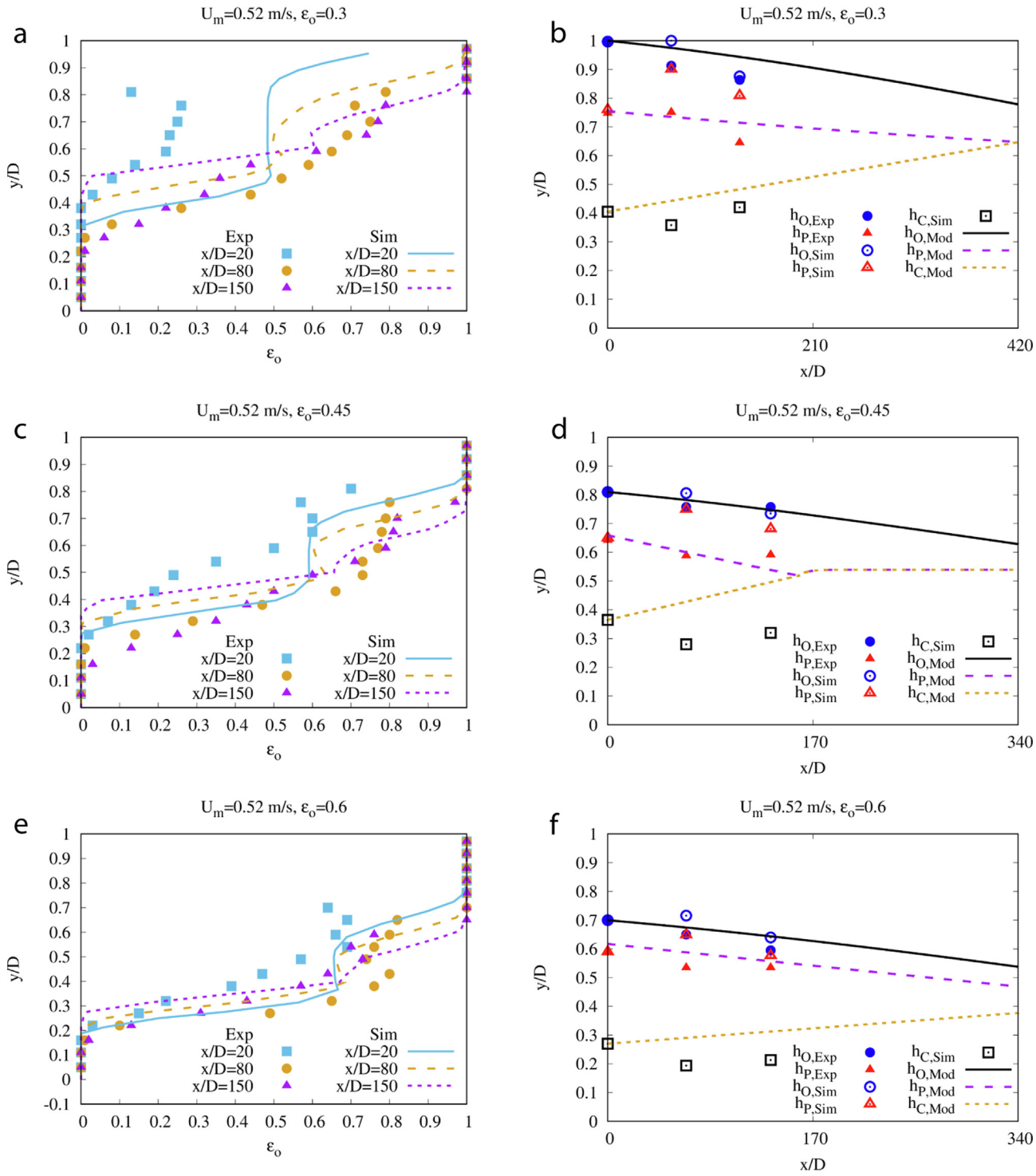

Fig. 9. Concentration profiles and layer heights for the cases of U_m = 0.52 m/s, d_w = 0.25 mm. The mechanistic model adopts parameters of d_{320} = 0.1 mm for ϵ_o = 0.3 and d_{320} = 0.2 mm for ϵ_o = 0.45, 0.6.

between the experiments, simulations, and the mechanistic model. However, the simulated h_C values differ from the model lines at the lower input oil concentration cases. This inconsistency between the concentration profiles and layer heights necessitates further investigation with the simulations.

3.2. Influence of the turbulent dispersion force

Regarding the deviation in the previous results, the turbulent dispersion force is added in the force models. Turbulent dispersion force considers the process that the particles were caught up in continuous phase turbulent eddies, and then carried from high concentration to low concentration regions. Lopez de Bertodano (1992) proposed a volume fraction based gradient model (Eq. 8), where C_{TD} is an empirical constant and C_{TD} = 0.1 to 0.5 might be suitable for medium sized fluid particles. Nevertheless, there is another framework for modelling the turbulent dispersion force in various multiphase flows (Gosman et al., 1992; Burns et al., 2004; Fox, 2014), which was based on the Favre averaging of the equations and finally correlated with the drag force. Both the tur-

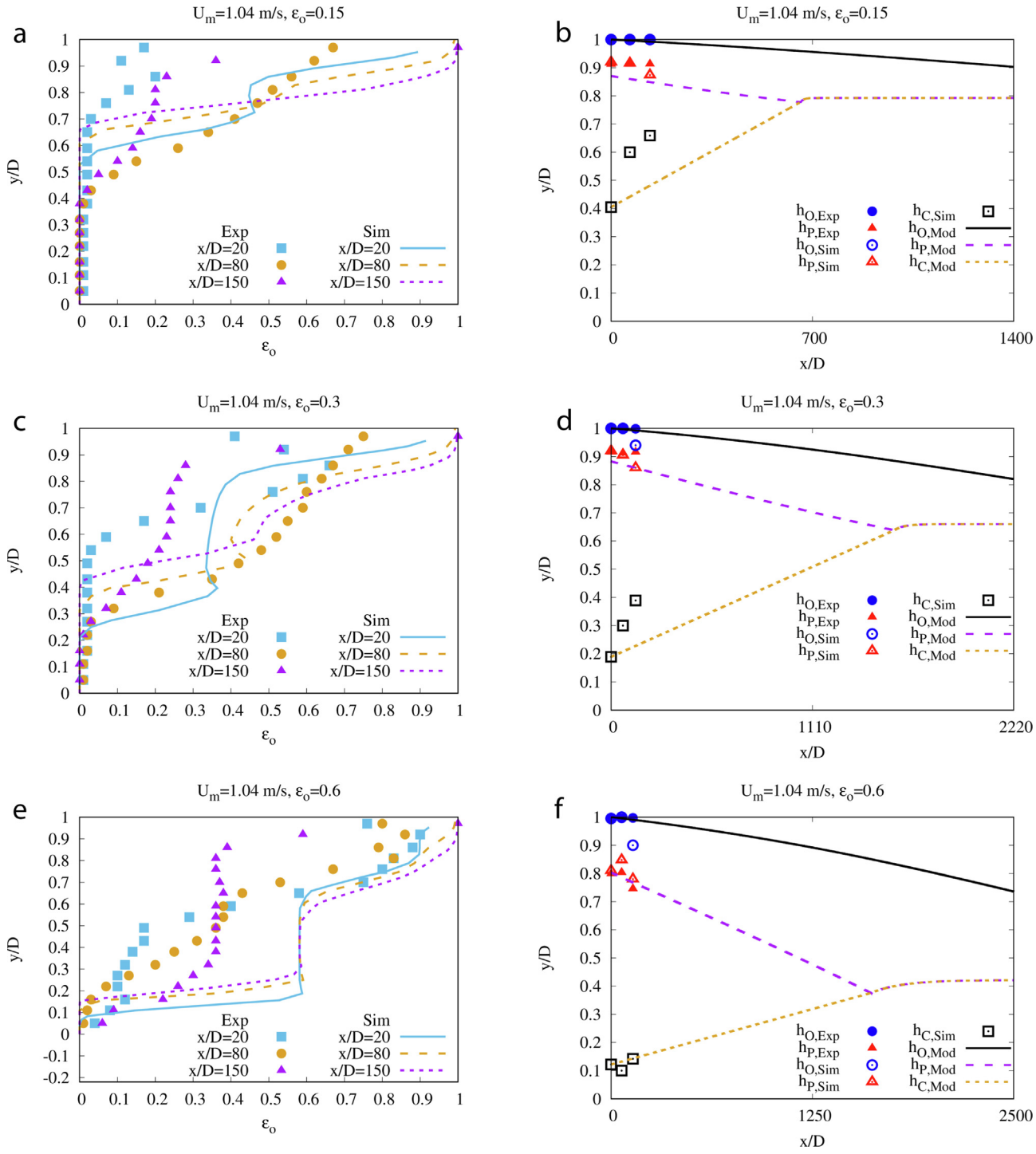

Fig. 10. Concentration profiles and layer heights for the cases of U_m = 1.04 m/s, d_w = 0.25 mm. The mechanistic model adopts parameters of d_{320} = 0.1 mm for ϵ_o = 0.15, 0.3 and d_{320} = 0.2 mm for ϵ_o = 0.6.

bulent dispersion force models of Lopez de Bertodano (1992) and Burns et al. (2004) are available in the OpenFOAM solver. At first, the Lopez de Bertodano model with $C_{TD} = 1$ was used as recommended in the literature (Wang and Yao, 2016; Pouraria et al., 2021), however, the predicted concentration profiles indicated that the dispersion effect was overestimated for this flow system. So a modified version of Eq. (8) was adopted by multiplying it with the local volume fraction of the dispersed phase, which is also a built-in model. This correction leads to a reduced turbulent dispersion force in comparison to the original Lopez de Bertodano model depending on the local volume fractions. As shown in Fig. 11, adding the turbulence dispersion force blurs the interface separating the two phases in the middle and downstream positions but has little effect on the concentration profiles near the pipe inlet.

For the lower velocity cases shown in Fig. 12, the predicted concentration profiles agree with the measurements well, especially for the middle and downstream positions. The predicted layer heights of h_O and h_P are higher than the measurements, leading to a much slower separation rate than the same cases without the dispersion force. However, the predicted layer heights of h_C

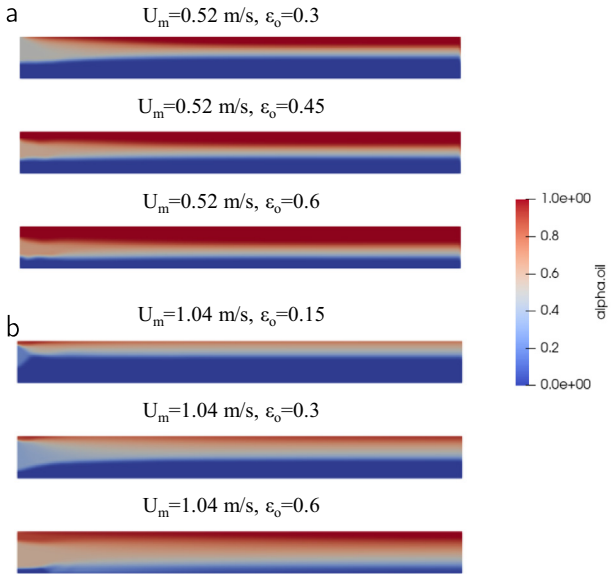

Fig. 11. Parametric dependence of the oil concentration profiles in the pipe on ϵ_o for $U_m = 0.52$ m/s, (a), and 1.04 m/s, (b), d_w = 0.5 mm, and in the presence of the turbulent dispersion force.

deviate from the anticipated rising trend along the flow direction, and the values for x/D = 80 and x/D = 150 are almost identical, which might be caused by the overestimated dispersion effect.

For the higher velocity cases shown in Fig. 13, it is interesting that the concentration profiles change significantly. Although there are still visible discrepancies, the predicted profiles are within the range of the experimental results, especially in the lower concentration cases of ϵ_o = 0.15 and 0.3. In addition, the correction is strong for the case of ϵ_o = 0.6, showing non-zero oil concentrations at the bottom region, as seen in Fig. 13(e), in agreement with the experiments. The predicted layer heights of h_O and h_P agree well with the experiments as well as the mechanistic model, while the trend of h_C cannot be well captured in these cases. In other words, although adding the turbulent dispersion force improves the prediction of concentration profiles, it is still unsatisfactory for the layer height predictions.

These results reveal that the turbulent dispersion force can also impact the flow pattern and the separation characteristics, and its effect is more obvious at higher velocities, which is reasonable because stronger turbulence should exist in those cases. Special attention should be paid to the two downstream positions, where identical values of the predicted h_C are observed in all the cases, while predictions of h_P and h_O are also very close for these two positions except in Fig. 13(f). It was expected that the model of Burns et al. (2004) can provide better predictions, however, very similar results were obtained by using that model, as shown in Fig. 14. Although there are some differences between Fig. 14 and Fig. 13, the predicted trends are qualitatively consistent. Hence, this study demonstrates that apart from the blending treatment, the turbulent dispersion force is another influential factor in the simulations, and no general rules are available to achieve excellent predictions in all aspects of the experimental data.

3.3. Discussion

The aforementioned results demonstrate that predicting the separation process requires an in-depth understanding of the complex flow behaviour. Droplet coalescence during the phase inversion and the existence of the DPL are crucial in this problem. The DPL is located between the flotation layer and the continuous oil layer, containing many accumulated oil droplets. It can be regarded as a mesoscale structure in the flow system, in which the separation depends on the complex coalescence process and the interaction with its adjacent layers due to their distinct moving conditions. To complete the coalescence at the interface close to the oil bulk phase, the water inside the DPL needs to be drained. The coalescence behaviour of these droplets is very different from that in a dilute system. Therefore, the traditional coalescence kernels are not sufficiently reliable to describe this behaviour, which is corroborated by the various drag corrections in the simulating work (Panjwani et al., 2015; Oshinowo et al., 2016). In other words, the significant viscosity increase in the continuous phase means that the apparent rising velocity of the droplets is reduced drastically.

Although the PBM model is adopted to describe the polydisperse droplet size distribution, it may face some deficiency when correcting the drag only by adjusting the mean diameter. For instance, there is a paradox of doing this in the present flow system. On the one hand, the experimental observation shows that hardly any breakage happens in this low turbulent flow and the Sauter mean diameter increases along the flow direction. On the other hand, since the droplet size in the present system is larger than general studied cases with $O\left(\sim 10^2 \mu\text{m}\right)$, even if constant values of the initial diameter in Table 2 are used in the simulation, the predicted separation will still be too fast in comparison to the physical process.

On the contrary, a blending-type treatment can reflect the phase-inversion induced delay of separation well. First, the impact of phase inversion on the continuous phase viscosity is delineated by the solver automatically in the local cells, which avoids *a priori* parameter fitting before the simulation. Second, the hindering effect of the DPL upon the coalescence rate can be determined by d_w which is about one order of magnitude smaller than the oil droplet. Although d_w is artificial in the present simulations, it reveals the necessity of correcting the momentum exchange when modelling and simulating the separation process. Factors of droplet settling (Evripidou et al., 2022), possible water drainage during the oil droplet coalescence (Cohen et al., 2015), and especially the complex droplet interactions in the DPL, would all contribute to the complex behaviour and provide various strategies to cope with this issue. Inspired by the blending treatment, if we can correlate the water holdup and some structural parameters in the DPL with the local flow fields, the local d_w values can be also determined automatically by the solver, then it is expected to improve the predicting accuracy in various cases.

Apart from the blending treatment, introducing a suitable turbulent dispersion force can also reduce the discrepancy between the predictions and the experiments, especially for higher velocity cases. The present model of turbulent dispersion force improves the prediction of concentration profiles but worsen that of phase separation. A mechanistic model must be developed to determine

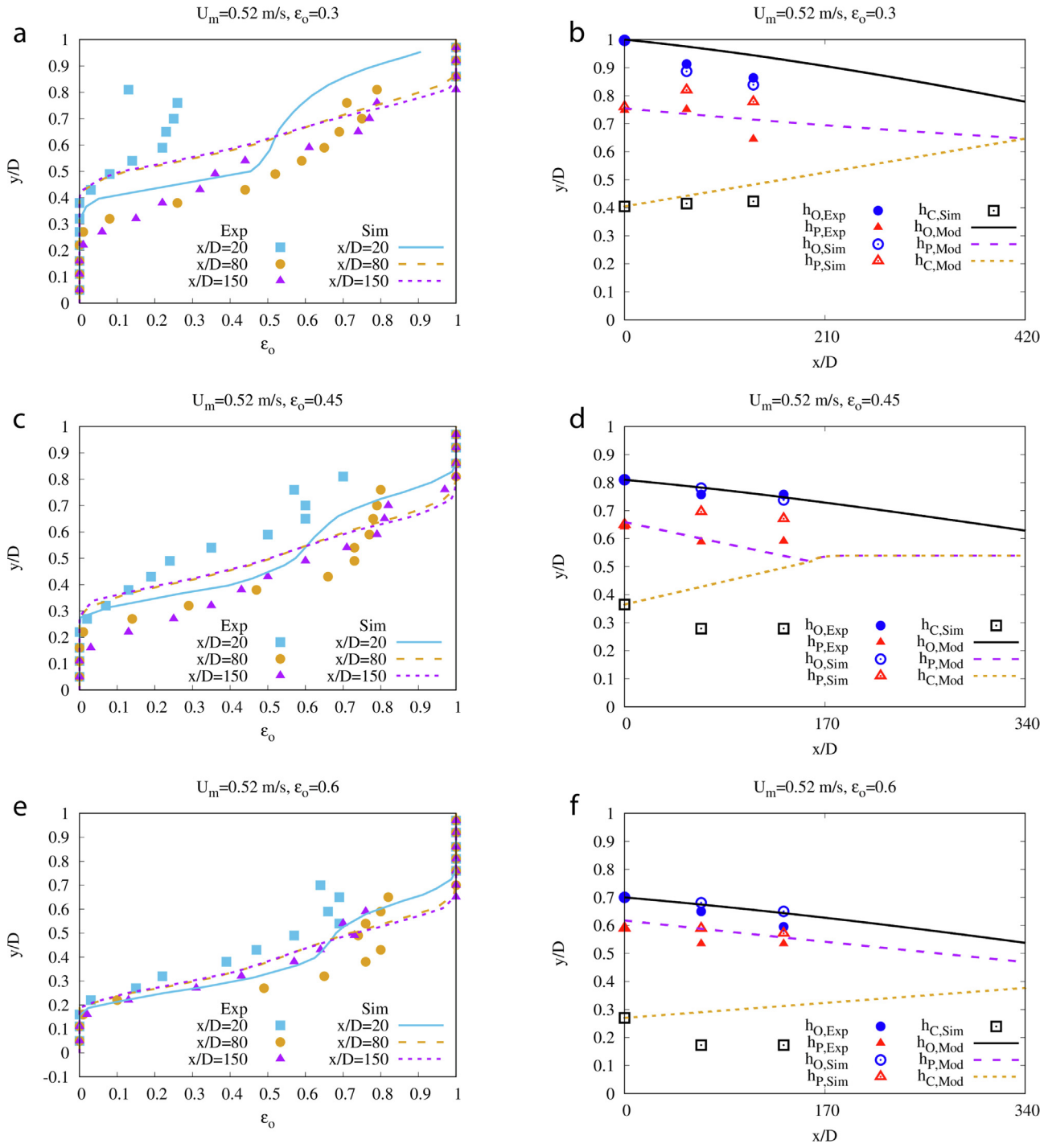

Fig. 12. Concentration profiles and layer heights for the cases of U_m = 0.52 m/s, d_w = 0.5 mm with the turbulent dispersion force. The mechanistic model adopts parameters of d_{320} = 0.1 mm for ϵ_o = 0.3 and d_{320} = 0.2 mm for ϵ_o = 0.45, 0.6.

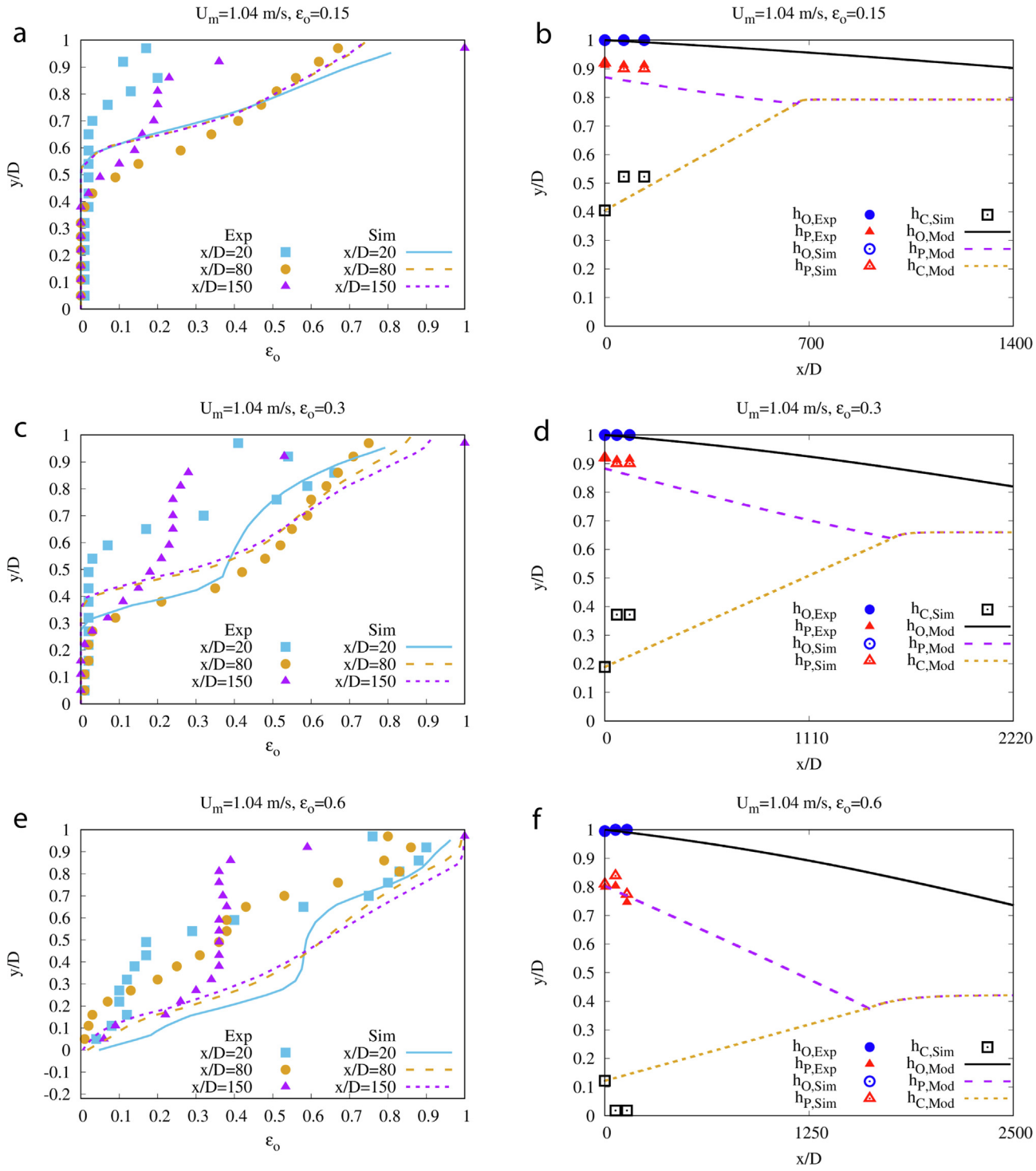

Fig. 13. Concentration profiles and layer heights for the cases of U_m = 1.04 m/s, d_w = 0.5 mm with the turbulent dispersion force (Lopez De Bertodano model). The mechanistic model adopts parameters of d_{320} = 0.1 mm for ϵ_o = 0.15, 0.3 and d_{320} = 0.2 mm for ϵ_o = 0.6.

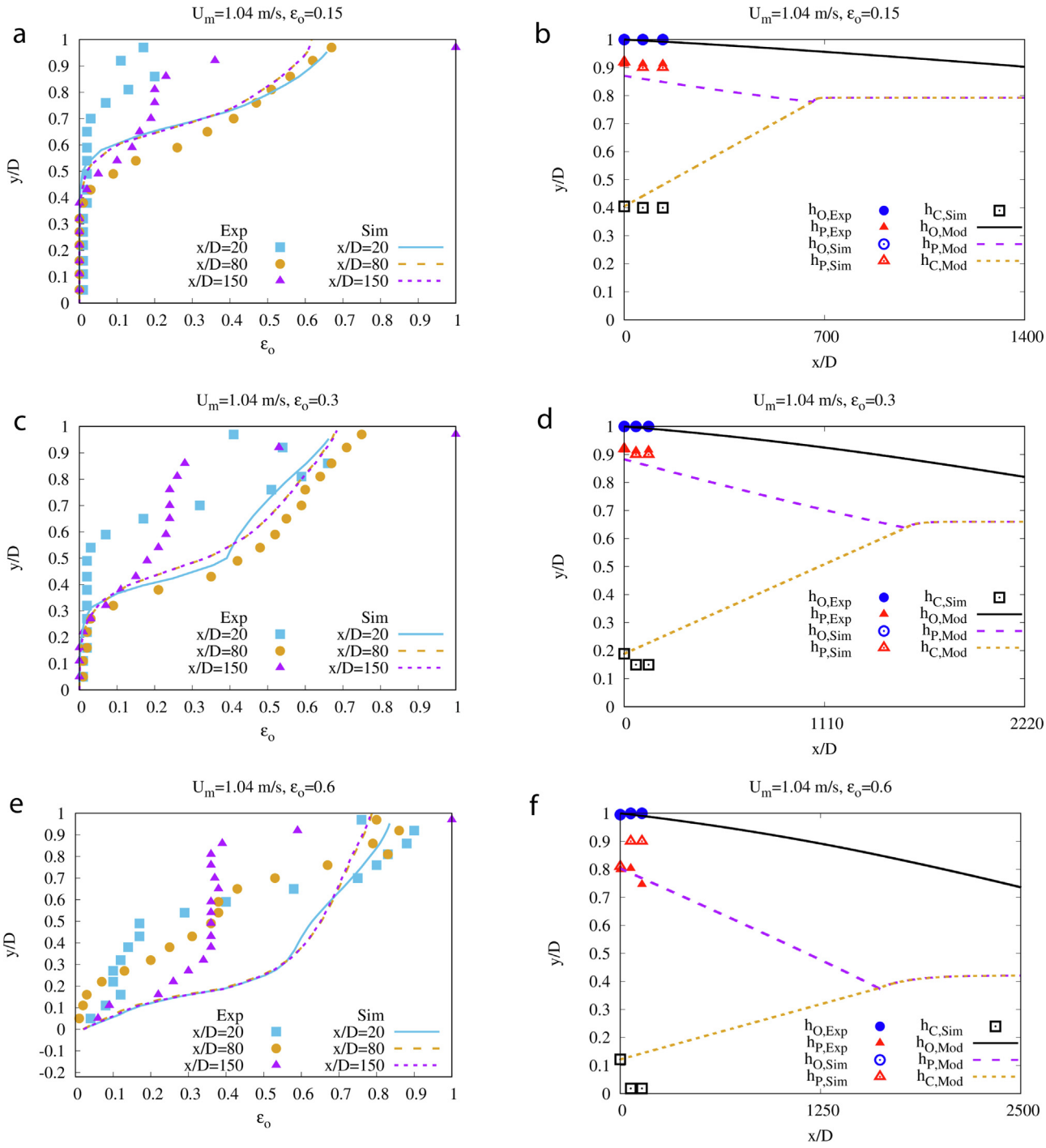

Fig. 14. Concentration profiles and layer heights for the cases of U_m = 1.04 m/s, d_w = 0.5 mm with the turbulent dispersion force (Burns model). The mechanistic model adopts parameters of d_{320} = 0.1 mm for ϵ_o = 0.15, 0.3 and d_{320} = 0.2 mm for ϵ_o = 0.6.

the continuous phase diameter of d_w so that the CFD framework developed here can enable satisfactory predictions of the oil–water separation characteristics in the pipe flow, with the least effort by reducing the trial-and-error cost. Furthermore, the CFD work can be combined with the data-driven models to obtain a quick prediction of the flow pattern and regime transitions in these flow systems, as demonstrated by our preliminary work (Cheng et al., 2022).

4. Conclusions

In this work, Eulerian-Eulerian simulations of an oil-in-water dispersed flow have been carried out. The distribution of the four layers that form was explored, and the simulation results of concentration profiles and layer heights were compared with experimental data. The blending treatment in the OpenFOAM solver has been shown to impact the simulated separation characteristics significantly. The sensitivity of results to the diameter of the original continuous phase was also studied thoroughly. Given that the droplet Sauter mean diameter in the present flow system, traditional breakup and coalescence kernels cannot reflect the real separation characteristics. Therefore, the blending treatment provides a feasible mechanism to correct the momentum exchange. Including the turbulent dispersion force in the modelling improved the prediction of concentration profiles, especially for the cases with higher velocity and lower concentration but the prediction of phase separation along the flow direction deteriorated, showing almost identical distributions for the downstream positions. It is still an open issue how to model the turbulent dispersion force in the simulation for different flow systems. In addition, the results were also compared against a mechanistic model, demonstrating that a correction of the initial Sauter mean diameter is needed to obtain reasonable predictions; this also supports the rationale of the blending treatment. The factors of phase inversion and the water release rate in the densely packed layer need further study so that improved drag and coalescence models can be proposed and embeded within the CFD simulations. Also, both interface-resolved simulations of the DPL and experimental work focusing on drop-interface coalescence deserve further exploration in future work.

Declaration of Competing Interest

The authors declare that they have no known competing financial interests or personal relationships that could have appeared to influence the work reported in this paper.

Acknowledgements

This work is supported by the Engineering and Physical Sciences Research Council, United Kingdom, the EPSRC PREMIERE (EP/T000414/1) Programme Grant, CAS and UCL scholarships, and the National Natural Science Foundation of China (NSFC) under Grant No. 22078327. The authors appreciate the helpful discussions with Profs. Benoit Chachuat, Mark Simmons, Federico Galvanin, and Nina Kovalchuk in the PREMIERE Team. JC also thanks Prof. Jinghai Li for his insightful instruction of the mesoscale method.

Appendix A. Equations of Pereyra's model

Note: Equations of (Pereyra et al., 2013; Pereyra, 2011) are given as below with two slight modifications in the present work, that is, the coefficient in Eq. (A15) is changed from 0.3025 to 0.2, and Eq. (A20) is replaced by $\epsilon_{P0} = 0.9$. These changes are arbitrary to obtain better predictions of the data.

In the following equations, $D\text{-}h_D, D - h_D - h_P$ and h_C correspond to the layer heights of h_O, h_P, h_C respectively in the present work.

(1) Sedimentation/flotation analysis:

$$h_C = \frac{v_S x}{u_M} \tag{A1}$$

$$v_S = \frac{3\lambda\epsilon\mu_C}{C_w\xi(1-\epsilon)\rho_C d_{320}}\left[\left(1 + Ar\frac{C_w\xi(1-\epsilon)^3}{54\lambda^2\epsilon^2}\right)^{0.5} - 1\right] \tag{A2}$$

$$Ar = \frac{\rho_C\Delta\rho g d_{320}^2}{\mu_C^2} \tag{A3}$$

$$\xi = 5K_{HR}^{-3/2}\left(\frac{\epsilon}{1-\epsilon}\right)^{0.45} \tag{A4}$$

$$K_{HR} = \frac{3(\mu_C + \mu_D)}{2\mu_C + 3\mu_D} \tag{A5}$$

$$\lambda = \frac{1-\epsilon}{2\epsilon K_{HR}}\exp\left(\frac{2.5\epsilon}{1-0.61\epsilon}\right) \tag{A6}$$

$$C_w = \frac{Ar}{6Re_\infty^2} - \frac{3}{K_{HR}Re_\infty} \tag{A7}$$

$$Re_\infty = \frac{\rho_C v_S^\infty d_{320}}{\mu_C} = 9.72\left[(1 + 0.01Ar)^{4/7} - 1\right] \tag{A8}$$

(2) Coalescence analysis:

$$u_M\frac{dh_D}{dx} = \frac{2\epsilon_I d_{32}^I}{3\tau_I} \tag{A9}$$

$$u_M\frac{d(d_{32})}{dx} = \frac{d_{32}}{3\tau_C} \tag{A10}$$

$$\tau_C = \frac{(6\pi)^{7/6}\mu_C r_a^{7/3}}{4\sigma^{5/6}H^{1/6}r_{F,C}r_v^*} \tag{A11}$$

$$\tau_I = \frac{(6\pi)^{7/6}\mu_C r_a^{7/3}}{4\sigma^{5/6}H^{1/6}r_{F,I}r_v^*} \tag{A12}$$

$$H = 1.0\times10^{-20} \tag{A13}$$

$$r_v^* = 0.007 \tag{A14}$$

$$r_{F,C} = 0.3025 d_{32}\sqrt{1 - \frac{4.7}{La + 4.7}} \tag{A15}$$

$$r_{F,I} = \sqrt{3}r_{F,C} \tag{A16}$$

$$rr_a = 0.5 d_{32}\left(1 - \sqrt{1 - \frac{4.7}{La + 4.7}}\right) \tag{A17}$$

$$La = \left(\frac{|\rho_C - \rho_D|g}{\sigma}\right)^{0.6} h_P^{0.2} d_{32} \tag{A18}$$

(3) Mass balance:

$$A_P = \begin{cases} \frac{A_C\epsilon - (1-\epsilon)A_D}{\epsilon_{P0} - \epsilon} & 0 < x \leqslant x_M \\ \frac{A_S\epsilon - A_D}{\overline{\epsilon}_P} & x > x_M \end{cases}, \tag{A19}$$

$$\epsilon_{P0} = \frac{1}{2}(\epsilon_I + \epsilon) \tag{A20}$$

$$\epsilon_I = 1.0 \tag{A21}$$

$$\overline{\epsilon}_P = \epsilon_I - \exp\left(-C_1\frac{x}{u_M} - C_2\right) \tag{A22}$$

$$C_1 = \frac{\overline{\epsilon}_P^2\Psi}{(A_S\epsilon - A_D)(\epsilon_I - \epsilon)} \tag{A23}$$

$$C_2 = -C_1\frac{x_{IN}}{u_M} - \ln(\epsilon_I - \epsilon) \tag{A24}$$

$$\Psi = \left[\frac{\partial A_P}{\partial h_P}\left(v_S + u_M\frac{dh_D}{dx}\right) - \frac{u_M}{\overline{\epsilon}_{P0}}\frac{\partial A_D}{\partial h_D}\frac{dh_D}{dx} - u_M\frac{\partial A_P}{\partial h_D}\frac{dh_D}{dx}\right]_{x=x_{IN}} \tag{A25}$$

(4) Geometrical correlations:

$$A_C = \frac{D^2}{4}\left[\pi - \cos^{-1}(\omega_C) + (\omega_C)\sqrt{1-(\omega_C)^2}\right] \quad (A26)$$

$$\omega_C = \frac{2h_C}{D} - 1 \quad (A27)$$

$$A_D = \frac{D^2}{4}\left[\pi - \cos^{-1}(\omega_D) + (\omega_D)\sqrt{1-(\omega_D)^2}\right] \quad (A28)$$

$$\frac{\partial A_D}{\partial h_D} = 2\sqrt{h_D(D-h_D)} \quad (A29)$$

$$\omega_D = \frac{2h_D}{D} - 1 \quad (A30)$$

$$A_P = \frac{D^2}{4}\left[\pi - \cos^{-1}(\omega_P) + (\omega_P)\sqrt{1-(\omega_P)^2}\right] - A_D \quad (A31)$$

$$\frac{\partial A_P}{\partial h_P} = 2\sqrt{(h_D+h_P)(D-h_D-h_P)} \quad (A32)$$

$$\frac{\partial A_P}{\partial h_D} = 2\sqrt{(h_D+h_P)(D-h_D-h_P)} - 2\sqrt{h_D(D-h_D)} \quad (A33)$$

$$\omega_P = \frac{2(h_D+h_P)}{D} - 1 \quad (A34)$$

References

Ahmed, S.A., John, B., 2018. Liquid-liquid horizontal pipe flow - A review. J. Petrol. Sci. Eng. 168, 426–447. https://doi.org/10.1016/j.petrol.2018.04.012.

Angeli, P., 1996. Liquid-liquid dispersed flows in horizontal pipes. Ph.D. thesis. Imperial College London.

Angeli, P., Hewitt, G.F., 2000. Drop size distributions in horizontal oil-water dispersed flows. Chem. Eng. Sci. 55, 3133–3143. https://doi.org/10.1016/S0009-2509(99)00585-0.

Antal, S.P., Lahey, R.T., J., Flaherty, J.E., 1991. Analysis of phase distribution in fully developed laminar bubbly two-phase flow. International Journal of Multiphase Flow 17, 635.

Behzadi, A., Issa, R.I., Rusche, H., 2004. Modelling of dispersed bubble and droplet flow at high phase fractions. Chem. Eng. Sci. 59, 759–770. https://doi.org/10.1016/j.ces.2003.11.018.

Bhusare, V.H., Dhiman, M.K., Kalaga, D.V., Roy, S., Joshi, J.B., 2017. CFD simulations of a bubble column with and without internals by using OpenFOAM. Chem. Eng. J. 317, 157–174. https://doi.org/10.1016/j.cej.2017.01.128.

Brauner, N., 2001. The prediction of dispersed flows boundaries in liquid–liquid and gas–liquid systems. Int. J. Multiph. Flow 27, 885–910. https://doi.org/10.1016/S0301-9322(00)00056-2.

Burns, A.D., Frank, T., Hamill, I., Shi, J.M., et al., 2004. The favre averaged drag model for turbulent dispersion in eulerian multi-phase flows, in: 5th international conference on multiphase flow, ICMF, pp. 1–17.

Chen, C., Guan, X., Ren, Y., Yang, N., Li, J., Kunkelmann, C., Schreiner, E., Holtze, C., Mülheims, K., Sachweh, B., 2019. Mesoscale modeling of emulsification in rotor-stator devices: Part I: A population balance model based on EMMS concept. Chem. Eng. Sci. 193, 171–183. https://doi.org/10.1016/j.ces.2018.08.048.

Cheng, J., Li, Q., Yang, C., Zhang, Y., Mao, Z., 2018. CFD-PBE simulation of a bubble column in OpenFOAM. Chin. J. Chem. Eng. 26, 1773–1784. https://doi.org/10.1016/j.cjche.2017.11.012.

Cheng, S., Chen, J., Anastasiou, C., Angeli, P., Matar, O.K., Guo, Y.K., Pain, C.C., Arcucci, R., 2022. Generalised latent assimilation in heterogeneous reduced spaces with machine learning surrogate models. Journal of Scientific Computing, in press. doi:10.1007/s10915-022-02059-4.

Cohen, A., Fraysse, N., Raufaste, C., 2015. Drop coalescence and liquid flow in a single Plateau border. Physical Review. E, Statistical, nonlinear, and soft matter physics 91,. https://doi.org/10.1103/PhysRevE.91.053008 053008.

Cunha, R.E.P., Fortuny, M., Dariva, C., Santos, A.F., 2008. Mathematical modeling of the destabilization of crude oil emulsions using population balance equation. Industrial & Engineering Chemistry Research 47, 7094–7103. https://doi.org/10.1021/ie800391v.

Deen, N.G., Solberg, T., Hjertager, B.H., 2001. Large eddy simulation of the gas-liquid flow in a square cross-sectioned bubble column. Chem. Eng. Sci. 56, 6341–6349. https://doi.org/10.1016/S0009-2509(01)00249-4.

Dong, T., Weheliye, W.H., Angeli, P., 2019. Laser induced fluorescence studies on the distribution of surfactants during drop/interface coalescence. Phys. Fluids 31, 12106. https://doi.org/10.1063/1.5059554.

Eskin, D., Vikhansky, A., 2019. Simulation of dispersion of stabilized water droplets in a turbulent oil flow through a horizontal tubing. Chem. Eng. Res. Des. 151, 261–269. https://doi.org/10.1016/j.cherd.2019.09.008.

Evripidou, N., Avila, C., Angeli, P., 2022. A mechanistic model for the prediction of flow pattern transitions during separation of liquid-liquid pipe flows. Int. J. Multiph. Flow 155, 104172. https://doi.org/10.1016/j.ijmultiphaseflow.2022.104172.

Fox, R.O., 2014. On multiphase turbulence models for collisional fluid–particle flows. J. Fluid Mech. 742, 368–424. https://doi.org/10.1017/jfm.2014.21.

Gosman, A.D., Lekakou, C., Politis, S., Issa, R.I., Looney, M.K., 1992. Multidimensional modeling of turbulent two-phase flows in stirred vessels. AIChE J. 38, 1946–1956. https://doi.org/10.1002/aic.690381210.

Grimes, B.A., 2012. Population balance model for batch gravity separation of crude oil and water emulsions. part I: Model formulation. J. Dispersion Sci. Technol. 33, 578–590. https://doi.org/10.1080/01932691.2011.574946.

Grimes, B.A., Dorao, C.A., Opedal, N.V.D.T., Kralova, I., Sørland, G.H., Sjöblom, J., 2012. Population balance model for batch gravity separation of crude oil and water emulsions. part II: Comparison to experimental crude oil separation data. J. Dispersion Sci. Technol. 33, 591–598. https://doi.org/10.1080/01932691.2011.574950.

Guitian, J., Joseph, D., 1998. How bubbly mixtures foam and foam control using a fluidized bed. Int. J. Multiph. Flow 24, 1–16. https://doi.org/10.1016/S0301-9322(97)00037-2.

Hartland, S., Jeelani, S.A.K., 1988. Prediction of sedimentation and coalescence profiles in a decaying batch dispersion. Chem. Eng. Sci. 43, 2421–2429. https://doi.org/10.1016/0009-2509(88)85176-5.

Henschke, M., Schlieper, L.H., Pfennig, A., 2002. Determination of a coalescence parameter from batch-settling experiments. Chem. Eng. J. 85, 369–378. https://doi.org/10.1016/S1385-8947(01)00251-0.

Hu, B., Matar, O.K., Hewitt, G.F., Angeli, P., 2006. Population balance modelling of phase inversion in liquid–liquid pipeline flows. Chem. Eng. Sci. 61, 4994–4997. https://doi.org/10.1016/j.ces.2006.03.053.

Ibarra, R., Matar, O.K., Markides, C.N., Zadrazil, I., 2015. An experimental study of oil-water flows in horizontal pipes, in: 17th International Conference on Multiphase Production Technology, BHR-2015-D2.

Ismail, A.S.I., Ismail, I., Zoveidavianpoor, M., Mohsin, R., Piroozian, A., Misnan, M.S., Sariman, M.Z., 2015. Review of oil-water through pipes. Flow Meas. Instrum. 45, 357–374. https://doi.org/10.1016/j.flowmeasinst.2015.07.015.

Jeelani, S.A.K., Hartland, S., 1985. Prediction of steady state dispersion height from batch settling data. AIChE J. 31, 711–720. https://doi.org/10.1002/aic.690310503.

Jeelani, S.A.K., Hartland, S., 1998. Effect of dispersion properties on the separation of batch liquid-liquid dispersions. Industrial & Engineering Chemistry Research 37, 547–554. https://doi.org/10.1021/ie970545a.

Jeelani, S.A.K., Panoussopoulos, K., Hartland, S., 1999. Effect of turbulence on the separation of liquid-liquid dispersions in batch settlers of different geometries. Industrial & Engineering Chemistry Research 38, 493–501. https://doi.org/10.1021/ie980436b.

Kamp, J., Villwock, J., Kraume, M., 2017. Drop coalescence in technical liquid/liquid applications: a review on experimental techniques and modeling approaches. Rev. Chem. Eng. 33, 1–47. https://doi.org/10.1515/revce-2015-0071.

Kharoua, N., Khezzar, L., Saadawi, H., 2013. CFD modelling of a horizontal three-phase separator: A population balance approach. American Journal of Fluid Dynamics 3, 101–118. https://doi.org/10.5923/j.ajfd.20130304.03.

Khatri, N.L., Andrade, J., Baydak, E.N., Yarranton, H.W., 2011. Emulsion layer growth in continuous oil-water separation. Colloids Surf., A 384, 630–642. https://doi.org/10.1016/j.colsurfa.2011.05.032.

Kopriwa, N., Buchbender, F., Ayesteran, J., Kalem, M., Pfennig, A., 2012. A critical review of the application of drop-population balances for the design of solvent extraction columns: I. concept of solving drop-population balances and modelling breakage and coalescence. Solvent Extr. Ion Exch. 30, 683–723. https://doi.org/10.1080/07366299.2012.700598.

Kumar, S., Ramkrishna, D., 1996. On the solution of population balance equations by discretization–II. a moving pivot technique. Chem. Eng. Sci. 51, 1333–1342. https://doi.org/10.1016/0009-2509(95)00355-X.

Lahey, J.R.T., 2005. The simulation of multidimensional multiphase flows. Nucl. Eng. Des. 235, 1043. https://doi.org/10.1016/j.nucengdes.2005.02.020.

Laleh, A.P., Svrcek, W.Y., Monnery, W.D., 2012. Design and CFD studies of multiphase separators–a review. Canad. J. Chem. Eng. 90, 1547–1561. https://doi.org/10.1002/cjce.20665.

Li, D., Christian, H., 2017. Simulation of bubbly flows with special numerical treatments of the semi-conservative and fully conservative two-fluid model. Chem. Eng. Sci. 174, 25–39. https://doi.org/10.1016/j.ces.2017.08.030.

Liao, Y., Lucas, D., 2010. A literature review on mechanisms and models for the coalescence process of fluid particles. Chem. Eng. Sci. 65, 2851–2864. https://doi.org/10.1016/j.ces.2010.02.020.

Liao, Y., Oertel, R., Kriebitzsch, S., Schlegel, F., Lucas, D., 2018. A discrete population balance equation for binary breakage. Int. J. Numer. Meth. Fluids 87, 202–215. https://doi.org/10.1002/fld.4491.

Lobo, L., Ivanov, I., Wasan, D., 1993. Dispersion coalescence: Kinetic stability of creamed dispersions. AIChE J. 39, 322–334. https://doi.org/10.1002/aic.690390212.

Lopez de Bertodano, M., 1992. Turbulent bubbly two-phase flow in a triangular duct. Ph.D. thesis. Rensselaer Polytechnic Institute.

Luo, H., Svendsen, H.F., 1996. Theoretical model for drop and bubble breakup in turbulent dispersions. AIChE J. 42, 1225–1233. https://doi.org/10.1002/aic.690420505.

Maluta, F., Buffo, A., Marchisio, D., Montante, G., Paglianti, A., Vanni, M., 2021. Effect of turbulent kinetic energy dissipation rate on the prediction of droplet size distribution in stirred tanks. Int. J. Multiph. Flow 136, 103547. https://doi.org/10.1016/j.ijmultiphaseflow.2020.103547.

Marschall, H., 2011. Towards the numerical simulation of multi-scale two-phase flows. Ph.D. thesis. Technische Universität München.
Nädler, M., Mewes, D., 1997. Flow induced emulsification in the flow of two immiscible liquids in horizontal pipes. Int. J. Multiph. Flow 23, 55–68. https://doi.org/10.1016/S0301-9322(96)00055-9.
Nguyen, H., Mohan, R., Shoham, O., Kouba, G., 2017. Droplet deposition and coalescence in curved pipes. Springer International Publishing, Cham., 187–199 https://doi.org/10.1007/978-3-319-59387-6_19.
Oshinowo, L.M., Quintero, C.G., Vilagines, R.D., 2016. CFD and population balance modeling of crude oil emulsions in batch gravity separation-comparison to ultrasound experiments. J. Dispersion Sci. Technol. 37, 665–675. https://doi.org/10.1080/01932691.2015.1054508.
Oshinowo, L.M., Vilagines, R.D., 2020. Modeling of oil-water separation efficiency in three-phase separators: Effect of emulsion rheology and droplet size distribution. Chemical Engineering Research & Design 159, 278–290. https://doi.org/10.1016/j.cherd.2020.02.022.
Panjwani, B., Amiri, A., Mo, S., Fossen, M., Linga, H., Pauchard, V., 2015. Dense packed layer modeling in oil-water dispersions: Model description, experimental verification, and code demonstration. J. Dispersion Sci. Technol. 36, 1527–1537. https://doi.org/10.1080/01932691.2014.1003221.
Pereyra, E., 2011. Modeling of integrated Compact Multiphase Separation System (CMSS©). Ph.D. thesis. The University of Tulsa.
Pereyra, E., Mohan, R.S., Shoham, O., 2013. A simplified mechanistic model for an oil/water horizontal pipe separator. Oil and Gas Facilities 2, 40–46.
Pouraria, H., Park, K.H., Seo, Y., 2021. Numerical modelling of dispersed water in oil flows using Eulerian-Eulerian approach and population balance model. Processes 9, 1345. https://doi.org/10.3390/pr9081345.
Prince, M.J., Blanch, H.W., 1990. Bubble coalescence and break-up in air-sparged bubble columns. AIChE J. 36, 1485–1499. https://doi.org/10.1002/aic.690361004.
Rusche, H., 2003. Computational fluid dynamics of dispersed two-phase flows at high phase fractions. Ph.D. thesis. Imperial College London.
Schumann, H., Tutkun, M., Nydal, O.J., 2016. Experimental study of dispersed oil-water flow in a horizontal pipe with enhanced inlet mixing, part 2: In-situ droplet measurements. J. Petrol. Sci. Eng. 145, 753–762. https://doi.org/10.1016/j.petrol.2016.06.022.
Shi, J., Gourma, M., Yeung, H., 2021. A CFD study on horizontal oil-water flow with high viscosity ratio. Chem. Eng. Sci. 229, 116097. https://doi.org/10.1016/j.ces.2020.116097.
Tomiyama, A., Tamai, H., Zun, I., Hosokawa, S., 2002. Transverse migration of single bubbles in simple shear flows. Chem. Eng. Sci. 57, 1849–1858. https://doi.org/10.1016/S0009-2509(02)00085-4.
Trallero, J.L., 1995. Oil-water flow patterns in horizontal pipes. Ph.D. thesis. The University of Tulsa.
Valdés, J.P., Asuaje, M., Ratkovich, N., 2021. Study of an ESP's performance handling liquid-liquid flow and unstable O-W emulsions part II: Coupled CFD-PBM modelling. J. Petrol. Sci. Eng. 198, 108227. https://doi.org/10.1016/j.petrol.2020.108227.
Voulgaropoulos, V., 2018. Dynamics of spatially evolving dispersed flows. Ph.D. thesis. University College London.
Wang, Q., Yao, W., 2016. Computation and validation of the interphase force models for bubbly flow. Int. J. Heat Mass Transf. 98, 799–813. https://doi.org/10.1016/j.ijheatmasstransfer.2016.03.064.
Wang, R., Zhang, B., Liu, C., Jiang, M., 2020. Physical modelling of dynamic evolution of metallurgical slag foaming. Exp. Thermal Fluid Sci. 113, 110041. https://doi.org/10.1016/j.expthermflusci.2020.110041.
Weber, M., 2021. Wattsapp in multiphase systems by gravity-driven buoyancy and settling. Chem. Ing. Tech. 93, 108–116. https://doi.org/10.1002/cite.202000103.
Weheliye, W.H., Dong, T., Angeli, P., 2017. On the effect of surfactants on drop coalescence at liquid/liquid interfaces. Chem. Eng. Sci. 161, 215–227. https://doi.org/10.1016/j.ces.2016.12.009.
Xu, X.X., 2007. Study on oil–water two-phase flow in horizontal pipelines. J. Petrol. Sci. Eng. 59, 43–58. https://doi.org/10.1016/j.petrol.2007.03.002.
Yu, H., Tan, C., Dong, F., 2020. Measurement of oil fraction in oil-water dispersed flow with swept-frequency ultrasound attenuation method. Int. J. Multiph. Flow 133, 103444. https://doi.org/10.1016/j.ijmultiphaseflow.2020.103444.
Zhou, H., Yu, X., Wang, B., Jing, S., Lan, W., Li, S., 2021. CFD-PBM simulation of liquid-liquid dispersions in a pump-mixer. Industr. Eng. Chem. Res. 60, 1926–1938. https://doi.org/10.1021/acs.iecr.0c05745.